RMZ

MATERIALS and GEOENVIRONMENT

MATERIALI in GEOOKOLJE

RMZ – M&G, **Vol. 68**, No. 2
pp. 1–50 (2021)

Ljubljana, December 2021

RMZ – Materials and Geoenvironment
RMZ – Materiali in geookolje
ISSN 1408-7073

Old title/Star naslov
Mining and Metallurgy Quarterly/Rudarsko-metalurški zbornik
ISSN 0035-9645, 1952–1997

Published by/Izdajatelj
Faculty of Natural Sciences and Engineering, University of Ljubljana/
Naravoslovnotehniška fakulteta, Univerza v Ljubljani

Associated Publisher/Soizdajatelj
Institute for Mining, Geotechnology and Environment, Ljubljana/
Inštitut za rudarstvo, geotehnologijo in okolje
Velenje Coal Mine/Premogovnik Velenje
Slovenian Chamber of Engineers/Inženirska zbornica Slovenije

Editorial Office/Uredništvo
Technical editors/Tehnična urednika Blaž Janc and Jože Žarn
Secretary/Tajnica Nives Vukič

Editorial Address/Naslov uredništva
RMZ – Materials and Geoenvironment
Aškerčeva cesta 12, p. p. 312
1001 Ljubljana, Slovenija
Tel.: +386 (0)1 470 46 10
Fax.: +386 (0)1 470 45 60
E-mail: bostjan.markoli@ntf.uni-lj.si
joze.zarn@ntf.uni-lj.si

Published/Izhajanje
4 issues per year/4 številke letno

Partly funded by Ministry of Education, Science and Sport of Republic of Slovenia./Pri financiranju revije sodeluje Ministrstvo za izobraževanje, znanost in šport Republike Slovenije.

Articles published in Journal "RMZ M&G" are indexed in international secondary periodicals and databases:/Članki, objavljeni v periodični publikaciji „RMZ M&G", so indeksirani v mednarodnih sekundarnih virih:
CA SEARCH® – Chemical Abstracts®, METADEX®, GeoRef.

The authors themselves are liable for the contents of the papers./
Za mnenja in podatke v posameznih sestavkih so odgovorni avtorji.

Annual subscription for individuals in Slovenia: 20 EUR, for institutions: 30 EUR. Annual subscription for the rest of the world: 30 EUR, for institutions: 50 EUR/Letna naročnina za posameznike v Sloveniji: 20 EUR, za inštitucije: 30 EUR. Letna naročnina za tujino: 30 EUR, inštitucije: 50 EUR

Transaction account/Tekoči račun
Nova Ljubljanska banka, d. d., Ljubljana: UJP 01100-6030708186

VAT identification number/Davčna številka
24405388

Online Journal/Elektronska revija
https://content.sciendo.com/view/journals/rmzmag/rmzmag-overview.xml?result=4&rskey=iClOT4#

Table of Contents

Kazalo

Original scientific Article
Izvirni znanstveni članki

Original Scientific Article • DOI: 10.2478/rmzmag-2021-0012

Received: January 07, 2021
Accepted: June 12, 2021

Determining the Enthalpy of an Fe-Ni Alloy at Various Temperatures Using the 'STA' PT 1600 Equipment

Določanje entalpije pri različnih temperaturah za zlitino Fe-Ni z napravo 'STA' PT 1600

Zarife Bajraktari-Gashi[1,*], Izet Ibrahim[1], Erard Morina[2]

[1]Faculty of Geoscience, Department of Materials and Metallurgy, University of Mitrovica "Isa Boletini", St. Ukshin Kovacica, 40000, Mitrovica, Republic of Kosovo

[2]NewCo Ferronikeli Complex L.L.C., St. Besim Mala no.227, 13000 Gllogoc, Republic of Kosovo

*Corresponding author: E-mail: zarife.bajraktari-gashi@umib.net

Abstract in English

In this research paper we have determined the enthalpy of the Fe-Ni alloy using the 'STA' equipment at the laboratory of the University of Mitrovica "Isa Boletini", Department of Materials and Metallurgy. The sample for analysis was taken at the Ferronikel plant, whereas the preparation of the sample for analysis on the 'STA PT 1600' equipment took place at the laboratory of the University of Mitrovica 'Isa Boletini'.

The sample of the Fe-Ni alloy analysed was 2–4 cm in size, in the shape of a granule. It contained, 22.55% Ni, 76.51% Fe, and small amounts of other elements [1, 2]. During the analysis of the Fe-Ni alloy, we obtained three enthalpy values under analytical conditions that included a maximum temperature of 800 °C and a minimum temperature of 600 °C; the alloy was exposed to each temperature separately for 45 minutes at each temperature.

The results showed negative enthalpy values during the three scenarios examined and an exothermic process where $\Delta H<0$ [3]. The enthalpy decreases as the system releases heat with an increase in temperature [4].

Keywords: STA, alloy, Fe-Ni, enthalpy, exothermic process

Abstract in Povzetek

V tem raziskovalnem prispevku smo določili entalpijo zlitine Fe-Ni z uporabo naprave 'STA' laboratorija Univerze v Mitrovici 'Isa Boletini', Oddeleka za materiale in metalurgijo. Vzorec za analizo je bil odvzet v tovarni ferroniklja, medtem ko je priprava vzorca za analizo na napravi 'STA PT 1600' potekala v laboratoriju Univerze v Mitrovici 'Isa Boletini'.

Analiziran vzorec zlitine Fe-Ni v obliki granule je bil velikosti 2–4 cm. Vseboval je 22,55 % Ni, 76,51 % Fe in majhne količine drugih elementov [1, 2]. Pri analizi zlitine Fe-Ni smo dobili tri vrednosti entalpije glede na pogoje analize z maksimalno temperaturo 800 °C in minimalno temperaturo 600 °C, pri čemer je bila zlitina izpostavljena obema temperaturama posebej po 45 minut.

Iz dobljenih rezultatov smo zbrali negativne vrednosti entalpije v treh preučenih scenarijih in eksotermnem procesu, kjer je $\Delta H<0$ [3]. Entalpija se zmanjšuje, ko sistem sprošča toploto z naraščanjem temperature [4].

Ključnebesede: STA, zlitina, Fe-Ni, entalpija, eksotermni proces

Introduction

Production of Fe-Ni alloy is a difficult process, beginning with the treatment of Fe-Ni ore and involving use of a rotary kiln, an electrical furnace, and finally a converter for the refinement of the metal [1, 5]. The costs of fuel for the rotary kiln and the electricity for melting the calcine are high.

The TGA/DSC equipment measures the heat as well as the change in weight of a material as a function of temperature or time in a controlled environment. The simultaneous measurements of these characteristics not

only improve productivity, but also simplify the interpretation of results. The data obtained make it possible to differentiate between endothermic and exothermic processes that do not experience weight loss (melting and crystallisation) and those that do experience weight loss (reduction). The simultaneous thermic analyser LINSEIS STA PT 1600 can be used for determining coinciding differences in mass (Tg) and caloric reactions (DSC) of a sample in a 25°C to 1650° temperature range. This simultaneous thermic analyser delivers high accuracy and high resolution. The equipment used for this research is located at the Department of Materials and Metallurgy of the University of Mitrovica 'Isa Boletini' (UMIB) and has the following three sensors: TG, TG-DTA, and TG-DSC.

All of the LINSEIS thermo-analytic instruments are controlled from a personal computer (PC). The individual software modules function exclusively using the Microsoft operating system Windows. The software is made up of three modules: temperature control, data acquisition, and data evaluation. The 32-bit program encompasses all fundamental properties for preparing, executing, and evaluating an STA measurement. Thanks to our application experts and specialists, LINSEIS was able to develop a user-friendly, all-inclusive software.

The standard enthalpy of forming a compound is defined as the energy associated with the reaction to form the compound from its constituent elements [3, 4]. The standard enthalpy of formation is a basic thermodynamic property that determines its phase stability, which can be coupled with other thermodynamic data to calculate phase diagrams.

Materials and methods

We carried out the analysis of the Fe-Ni alloy at the Ferronikel plant's laboratory in Drenas and obtained the following composition expressed as the percentage of each element [2] (Table 1):

Table 1: *Composition of Fe-Ni alloy [2]*

Ni	Fe	S	C	Co	P	Si	Cr	Cu
22.55%	76.51%	0.12%	0.01%	0.75%	0.01%	0.01%	0.01%	0.03%

Figure 1: *View of a metal casting of refined Fe-Ni.*

Figure 2: *View of Fe-Ni alloy (granule) [2].*

Figure 3: *Preparation of the sample (UMIB).*

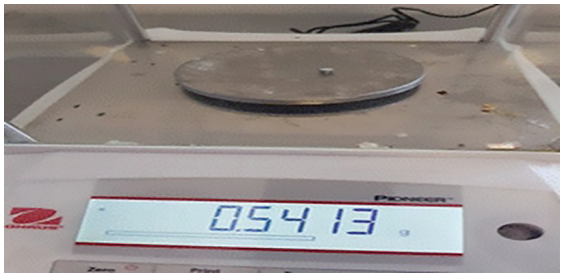

Figure 4: *Measuring weight of the sample on an analytical scale.*

The Fe-Ni alloy sample with the composition found in (Table 1) was prepared at the laboratory of UMIB Department of Materials and Metallurgy. For the preparation of the Fe-Ni alloy sample, we relied on the available parameters of the LINSEIS 'PT STA 1600'.

The sample has the following parameters:

- Length: 4 mm
- Width: 4 mm
- Weight: 0.5413 g

The sample was weighed on an analytical scale (Figure 4) at the laboratory of the Faculty of Food Technology (UMIB).

The Fe-Ni alloy sample, after polishing, was placed on the 'alumina' plate, and the conditions of the analysis were as follows:

- Maximum temperature = 800 ℃, for a duration of 45 minutes
- Minimum temperature = 600 ℃, for a duration of 45 minutes

The initial temperature is the initial extrapolated temperature of the reaction; the final temperature is the final extrapolated temperature of the reaction. In an exothermic reaction, energy is released because the total energy of the products is lower than the total energy of the reactants. As a result, the change in enthalpy, ΔH, for an exothermic reaction will always be negative. The heat variations in chemical reactions are often measured at the laboratory under conditions in which the reaction system is open to the ambient temperatures. In that case, the system is exposed to constant pressure.

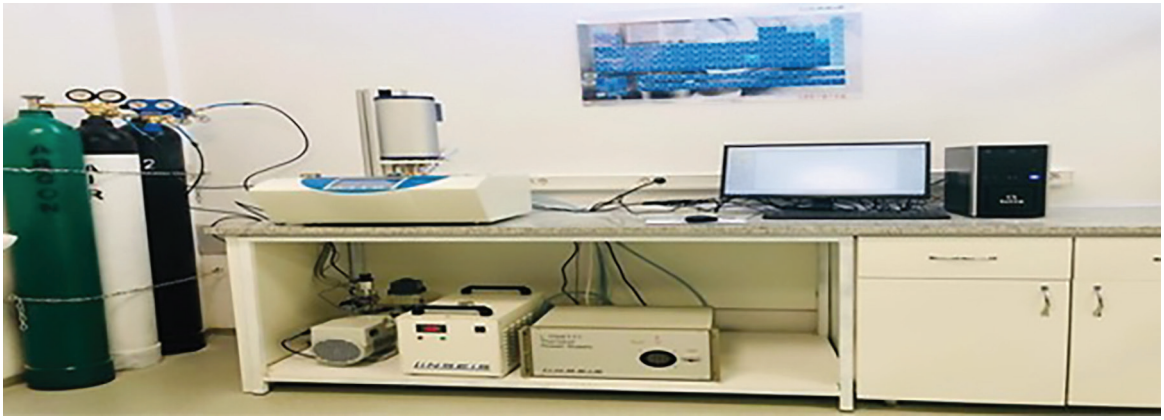

Figure 5: *LINSEIS PT 1600 (UMIB laboratory).*

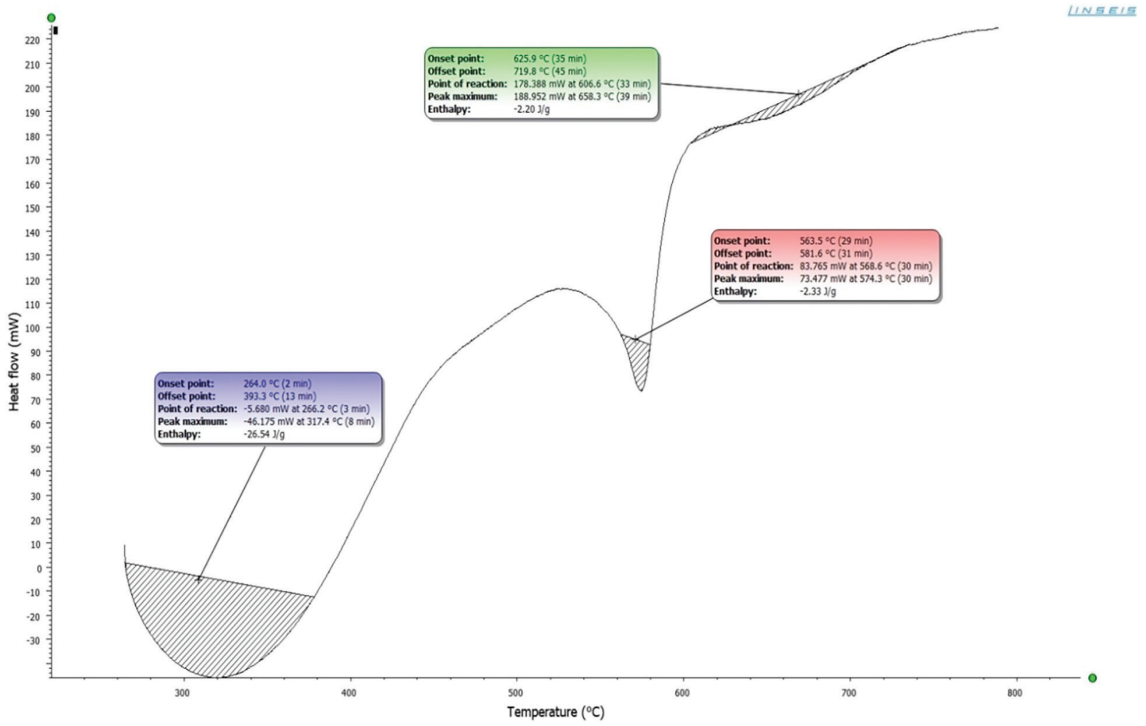

Figure 6: *Determination of the enthalpy of the Fe-Ni alloy in LINSEIS 'PT STA 1600' at UMIB.*

Chemists routinely evaluate changes in the enthalpy of chemical systems as the reactants are converted into products. The heat absorbed or released by a reaction at constant pressure is the same as the change in enthalpy and is identified by the symbol ΔH.

Discussion of results

Using the LINSEIS 'PT STA 1600' to analyse the Fe-Ni alloy, we have determined the enthalpy, which decreases as the temperature rises (ΔH<0), leading to the conclusion that these reactions are exothermic [3, 4]. Energy must be inserted into the system to break the chemical bonds, as they frequently do not break away spontaneously. The formation of bonds includes the release of energy; therefore, if more energy is produced in the formation of the bond than is necessary to break the bond, the enthalpy is negative—as we have found in the Fe-Ni alloy [3]. In this example, the change in enthalpy is negative because heat is released

from the system, causing the overall enthalpy of the system to decrease [3, 4].

The heat of the reaction is the change of enthalpy for a chemical reaction [3]. The determination of the enthalpy of the Fe-Ni alloy supports our conclusion that the Fe-Ni alloy is an appropriate product for the acquisition of special steels and other stable alloys [3, 4].

References

[1] Bajraktari-Gashi, Z., Zabeli, M., Halilaj, B. (2020): Key metallurgical parameters of Fe-Ni production during 1984–1997 and 2007–2017 at the Ferronickel smelter in Drenas. *Materials and Geoenvironment,* 67(2), pp. 73–77, DOI:10.2478/rmzmag-2020-0008.

[2] New Ferronickel Complex L.L.C. (1984–1997; 2016–2020). Official Documentation of Melting.

[3] Peter, A., Julio, D.P. (2006): *Physical Chemistry*. Oxford University Press: Oxford, 1000 pp.

[4] Shamsuddin, M. (2016): *Physical Chemistry of Metallurgical Processes, Second Edition*. John Wiley & Sons, Inc: New Jersey, 608 pp.

[5] Bajraktari-Gashi, Z., Halilaj, B. (2018): Material balance of the technological process in the new foundry of new Ferronikel in Drenas during 2017. *Journal of Technology and Exploitation in Mechanical Engineering*, 4(1), pp. 29–35, DOI:10.35784/jteme.90.

Original Scientific Article • DOI: 10.2478/rmzmag-2021-0008

Received: October 26, 2021
Accepted: December 06, 2021

Lateral squeezing effects on cement-slag-bentonite slurry wall performance

Davood Talefirouz[1,*], Erdal Çokça[2]
[1]Civil Engineering Department, Middle East Technical University, Ankara, Turkey
[2]Civil Engineering Department, Middle East Technical University, Ankara, Turkey
*Corresponding author: E-mail: talefirouz@gmail.com

Abstract in English

Cement-slag-bentonite slurry walls are self-hardening structures, and they are mainly used to retard contamination transport into the groundwater stream. Whilst permeability of a mixture is an initial criterion in slurry wall design and material selection, long-term performance is mainly influenced by curing ages and stress-state caused by adjacent soil. In this study, the steady-state of effective stresses at 7 days and 28 days of curing age is predicted. The effect of the modulus of horizontal subgrade reaction, interface friction, and transition of the earth pressure from at-rest to the active condition was applied to develop the model. Unlike the quantities that the geostatic model presented, this method gives a slight decrease of stresses after a certain depth, and the trend is in good agreement with trends provided by previous studies. Furthermore, the predicted stresses are then applied to estimate the permeability of the wall at each depth and compare it with those obtained in the laboratory. Finally, predicted effective stresses stay lower than geostatic stress, and the slurry wall consolidation along with the sidewalls' lateral squeezing leads to keeping the stress state under control.

Keywords: cement-slag-bentonite, compressibility; lateral squeezing, permeability, slurry wall

Introduction

Cement-slag-bentonite (CSB) slurry walls as nonstructural barrier techniques have been widely employed to decrease contaminants' migration into the groundwater stream. Within this area of consideration, a proper estimation of the wall permeability is an important parameter for the slurry wall design. For groundwater control applications, a permeability of 1×10^{-9} m/s is specified for CSB slurry walls, although a permeability of 1×10^{-8} m/s or higher would be sufficient for most remediation applications [1]. Even though the self-hardening property of the CSB mixture exerts effects on permeability reduction, several studies have also shown that permeability decreases as the weight of the joint increases [2-4]. Consequently, an appropriate prediction of the lateral earth pressure development within the slurry wall is important. The hypothesis of the lateral squeezing modeling was initially proposed by Filz [5], and this method for modeling was then developed by many researchers considering the arching and squeezing effect for deep trenches [6-8].

Observations differ for the analysis of the mechanism; however, the results of all approaches indicate that the stress state in the trench (below the depth of 5–7 m) remains lower than the geostatic approach. It has been suggested that the major principal stress in deep-narrow slurry walls is horizontal, and it is vertical in shallow-wide slurry walls [5, 9, 8]. However, the specific mechanism behind the lateral squeezing models [9, 5] has not been fully addressed for modeling of one sort or another. Proposed theories are based on the

assumption that either the earth pressure coefficient is in the at-rest condition for surrounding soils or neglects the down-drag force between the mixture placements and completed consolidation.

This paper describes a model to estimate effective stress in CSB slurry walls employed at 7 days and 28 days of curing ages based on laboratory consolidation and index tests. To consider both arching and lateral squeezing mechanisms, the method provided by Li et al. [6] is used to obtain major principal stress (horizontal stress) with depth. Earth pressure transition from at-rest to the active condition presented by Bang and Kim [10] is then applied to evaluate minor principal stress (vertical stress). Then, the permeability of the wall can be predicted based on obtained stresses at a given curing age and compared with those achieved in the laboratory for the same stress values.

Material and Methods

To identify the stress-state in a CSB slurry wall, two different mixtures with 20% of cementitious material mixed with 80% of the bentonite-water slurry are used. For the first mixture, ground granulated blast furnace slag (GGBS) is replaced with 50% cement type I by dry weight to make up the 20% of cementitious material. In this mixture, the bentonite-water slurry contains 5% of bentonite mixed into distilled water to make up the 80% batch slurry which is allowed to hydrate for one week. Hence, one kilogram of this mixture comprises the following: 100 g cement, 100 g GGBS, 40 g bentonite, and 760 g distilled water (C50-S50-B5). In the second mixture, 5% lime is employed for the cementitious mixture mentioned above and replaced with a 5% portion of GGBS as well as increasing the bentonite content of the batch slurry to 9%. Consequently, one kilogram of this mixture includes the following proportions: 100 g cement, 90 g GGBS, 10 g lime, 72 g bentonite, and 728 g distilled water (C50-S45-L5-B9). The following chemical reactions are expected among the materials in the mixture. The lime in a hydrated form ($Ca(OH)_2$) reacts with the montmorillonite structure containing alumino-silicates and also reacts with GGBS, which is a pozzolanic material and has CaO, SiO_2, and $Al2O_3$. These silica and aluminum particles react with lime in a hydrated structure to form calcium silicate hydrate (CSH), calcium aluminate silicate hydrate (CASH), and calcium aluminate hydrate (CAH), which are separated into gap minerals in response to calcium particles. CSA and CAH are cementitious objects, such as those in the form of a Portland concrete grid ($3CaO{\cdot}SiO_2$, $2CaO{\cdot}SiO_2$, $3CaO{\cdot}Al_2O_3$, $4CaO{\cdot}Al_2O_3{\cdot}Fe_2O_3$). The matrix formed is permanent. The state of stress in slurry walls depends on inward pressure from adjacent soils and the weight of the wall [5, 11]. A two-dimensional CSB slurry wall, with width and depth of B and H, respectively, surrounded by submerged medium dense sand, is investigated in this paper. It is assumed that the mixture placed into the trench along with the surrounding soils is homogeneous and isotropic, and the groundwater table is at the surface [5-8]. Since the horizontal strain of mixtures after placement is expected to be zero, the geometry of the problem is identified as plain-strain. Subsequently, in this two-dimensional coordinate system, inward horizontal deformation is assumed to be positive, and the ground surface is indicated as the origin of z (Figure 1). Consequently, in the following problem, the longitudinal direction implies the transverse direction. Once the fresh mixture is placed, it is assumed that the pore water pressure $u=\gamma_w z+\gamma'_{csb} z$ carries the self-weight of the CSB at depth z of the wall and at excess pore water pressure $u_e=\gamma'_{csb} z$, where γ_w and γ'_{csb} are the unit weight of water and floating unit weight of CSB, respectively, and the vertical and horizontal effective stress in the wall is $\sigma'_h=\sigma'_v=0$. During the consolidation procedure, the pore water pressure is intended to decline to hydrostatic pressure, and the magnitude of effective stresses need to be specified.

According to Filz [5], inward displacement of the trench sidewalls should take place to keep horizontal stress equilibrium applied to the sidewalls. Alternatively, the interface frictional

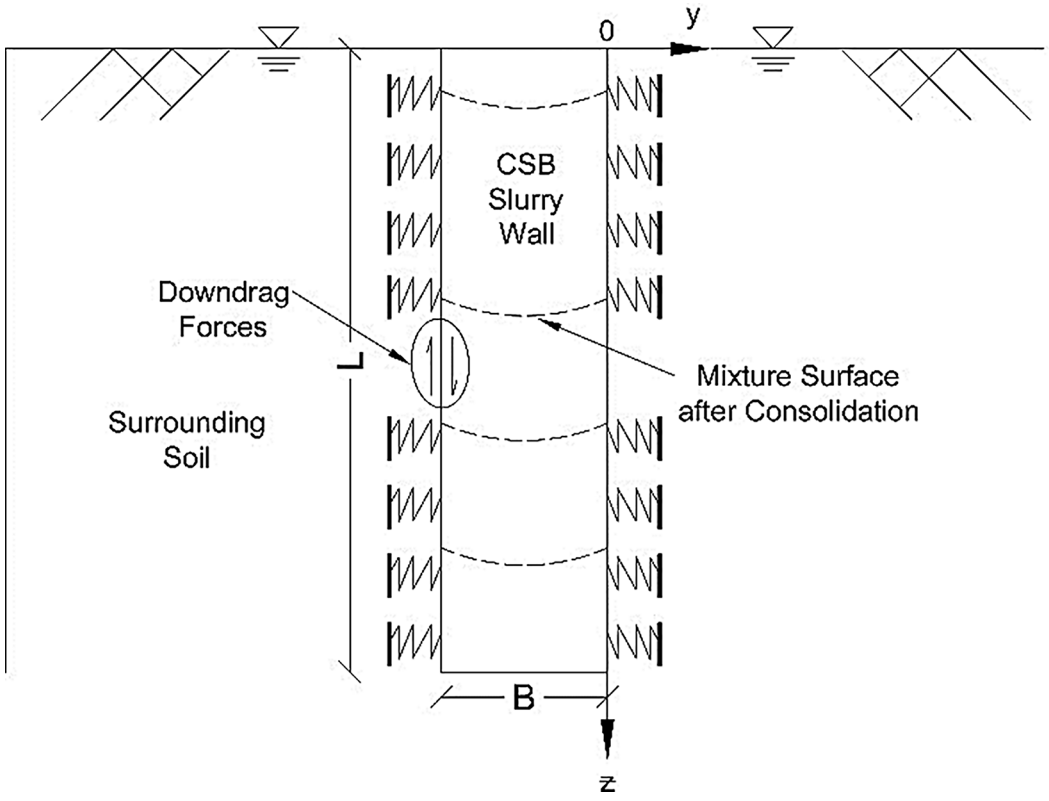

Figure 1: *Schematic of the sidewall friction on the stress distribution in a CSB slurry wall.*

stress τ between the trench wall and adjacent soil during the consolidation procedure [3, 6, 7] follows the Mohr-Coulomb strength criterion as

$$\tau = C'_{in} + \sigma'_h \tan \varnothing'_{in} \tag{1}$$

where C'_{in} and $\varnothing'_{in}$ are the solidity and internal friction angle of the sidewall interface, respectively, and as mentioned by Potyondy [12], the relationship is as follows

$$C'_{in} = RC'_{CSB} \tag{2}$$

and

$$tan\varnothing'_{in} = Rtan\varnothing'_{in} \tag{3}$$

where C'_{CSB}, $\varnothing'_{CSB}$, and R are the cohesion, internal friction angle, and shear strength reduction factor of the cured wall, respectively. It is assumed that effective horizontal stress at the ground surface and the top of the CSB wall is $\sigma'_h = 0$ at z = 0. A model proposed by Li et al. [6] for a lateral squeezing effect caused by the inward displacement of side walls is

$$\sigma'_h = \frac{B\gamma'_{CSB}}{2tan\varnothing'_{in}}\left(1 + A - \frac{2c'_{in}}{B\gamma'_{CSB}}\right) \times \left[1 - \exp\left(-\frac{2tan\varnothing'_{in}}{BD}z\right)\right] \tag{4}$$

where the coefficient of A and D can be outlined as

$$A = \frac{2E}{v(1+v)BK} \tag{5}$$

so that

$$D = \frac{1-v}{v} + A \tag{6}$$

According to Das [13], an elastic medium of soils can be expressed as a series of infinitely

elastic springs (Figure 1), and the subgrade module for cohesive soils at depth z can be characterized as

$$k_z = n_h z \tag{7}$$

where n_h is the constant of modulus of horizontal subgrade reaction. As reported by Filz [5], the following relationship between vertical and horizontal effective stress in the lateral squeezing model is

$$\sigma'_v = k_m \sigma'_h \tag{8}$$

where k_m is the coefficient of lateral earth pressure employed into the trench wall. The conventional consideration is that there is no need to evaluate wall-to-soil shear resistance or down-drag force when the coefficient of at-rest earth pressure is assumed for the surrounding soil [14]. However, during fresh mixture placement into the trench, the mixture will settle corresponding to the sidewall under its weight and deploys a down-drag force. This phenomenon then develops until consolidation completion. The role of an at-rest earth pressure condition in a slurry wall, that is, no inward displacement of surrounding soils into the trench, is assumed. Besides, Clough and Duncan [14] pointed out that where the proposed backfill material is cohesive, a moderate earth pressure between at-rest and active conditions must be mobilized for design. To illustrate lateral earth pressure transition from at-rest to active condition, a method proposed by Bang and Kim [10] is investigated to analyses the relationship between the major and minor principal effective stresses. Where k_0 is known as the coefficient of at-rest lateral earth pressure, the subsequent angle $\emptyset_0$ can be described as

$$\sin\phi_0 = \frac{1-k_0}{1+k_0} \tag{9}$$

where $k_0 = 1 - \sin\emptyset_0$, then

$$\sin\phi_0 = \sin\phi / (2 - \sin\phi) \tag{10}$$

If the angle, ψ, refers to the relationship between major (horizontal) and minor (vertical) principal effective stress, then considering a ψ value between Ø and $\emptyset_0$ describes a displacement angle for active and at-rest values, respectively. So, the intermediate part at each depth can be defined as $\emptyset_0 < \psi < \emptyset$. Furthermore, where δ is the cured slurry wall friction angle, so that;

$$\sin\Delta = \sin\delta / \sin\emptyset \tag{11}$$

Since ψ (z) can be used instead of Ø, and δ (z) is the developed cured slurry wall friction at depth z, Equation (11) can be modified to result in

$$\sin\Delta(z) = \left[\sin\delta(z) / \sin\psi(z)\right] \tag{12}$$

And the variation of δ (z) can be considered to be zero for at-rest and to be δ_{max} in an active condition. The average stress for plain-strain at any depth is

$$\sigma = \frac{\sigma_v + \sigma_h}{2} \tag{13}$$

Subsequently, the complete solution once σ along the ground surface up to the entire depth (z), that is, developed at the face of the slurry wall, the intermediate earth pressure coefficient can be analyzed from

$$km = \left[\sin\left(\Delta(z) - \delta(z)\right) / \sin\Delta(z)\right] \cos\delta(z) \,|\, z = z_y \tag{14}$$

However, Equation (14) requires detailed solution steps, which is a function of, ψ (z), and provides lateral earth pressure transition from at-rest to the active condition. The variation for ψ (z), is from $\emptyset_0$ for at-rest to Ø for active condition. In other words, if the stage of the sidewall from mixture placement to consolidation completion denotes β, then β=0 and β=1 can describe the at-rest and active conditions, respectively (Figure 2). Accordingly, the deformation development of the surrounding soils at z = 0 is $0 \le \beta \le 1$, whereas the variation of ψ (z) is assumed to be ψ (z) = Ø, and at z = H it is determined to be ψ (z) = $\emptyset_0$. So it can be expressed as

$$\psi(z) = \emptyset_0 + \left(\emptyset - \emptyset_0\right)\left(1 - \frac{z}{H}\right)\beta \tag{15}$$

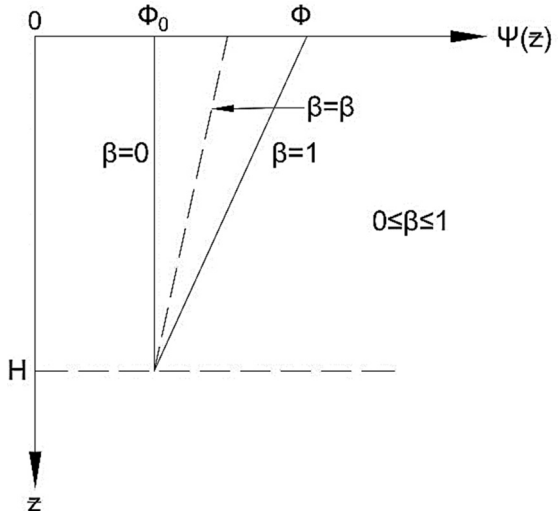

Figure 2: *Transition of ψ(z) from Ø 0 to Ø with depth [10].*

where

$$\frac{\partial\psi(z)}{\partial z} = -\beta\left(\varnothing - \varnothing_0\right)/H \tag{16}$$

Consequently, for β=0, at both depth z=0 and depth z=H, wall tilt is considered to be ψ(z) = $Ø_0$ and ψ(z) = Ø, respectively. The solution to β=β at depth z=0 can be expressed as $Ø_0$ < ψ(z) < Ø, and at depth z=H ψ(z) = $Ø_0$, ψ(z) decreases linearly between z=0 and z=H. Using β=1 at depth z=0 ψ(z)=Ø and at depth z=H ψ(z) = $Ø_0$, the variation of ψ(z) between z=0 and z=H reduces linearly.

Application and Validation

This section presents an assessment of the validity of the proposed model to a case of CSB slurry wall. A CSB is constructed to intercept and impede the stream of polluted fluids towards the groundwater. CSB provides lower structural strength compared to diaphragm and concrete walls. An alternative explanation might be that the CSB wall is principally constructed as a plastic medium with stress-strain properties much closer to the soil than concrete walls. Consequently, it should not be considered a structural wall, instead, the CSB slurry wall can be modeled as elastic soil [15]. On the basis of the relationship between stress and void ratio for CSB samples, Opdyke and Evans [1] concluded that the coefficient of consolidation (C_v) of 94×10^{-4} cm^2/s indicates the upper limit of natural clay soils, and the behavior is closely akin to overconsolidated soil. For remolded soils with liquid limits around 60%, Sridharan and Nagaraj [16] have provided an upper limit for the coefficient of consolidation of 3×10^{-4} cm^2/s. In addition, for marine clay treated with 8% lime and 20% slag, Rao and Raju [17] obtained a coefficient of consolidation of 5.17×10^{-4} cm^2/s. In this study, the time-rate of consolidation for CSB was investigated for loading increments from 200 kPa to 400 kPa. The laboratory experiment was conducted to investigate the consolidation parameters of the samples at 7 days and 28 days of curing time and other index properties (Table 1). Since the compressibility of CSB is similar to hard clay soil rather than a structural concrete wall, the authors decided to consider the performance of CSB as being similar to clay soil on the basis of elastic theory.

Laboratory datasets were assumed to apply on a site; that is, saturated medium dense sand encapsulated a trench with a width and a depth of 1.2 m and 30 m, respectively. The Poisson's ratio values were theoretically obtained for the samples at a given curing time and are related to Young's modulus *E* and elastic modulus K relationship, that is:

$$\mathrm{E} = 3\mathrm{K}\left(1-2\nu\right) \tag{17}$$

The Young's modulus *E* of mixtures at each curing age has the following relationship with constrained modulus D, corresponding to elastic theory

$$E = \frac{\left(1+\upsilon\right)\left(1-2\upsilon\right)}{1-\upsilon} D \tag{18}$$

where

$$D = \frac{\sigma'}{\varepsilon} \tag{19}$$

As the geotechnical status of the site shows, a direct relationship between the additional load module *k* and the depth is used with the normal estimate of n_h of submerged average thickness sand [13]. During the construction procedure, a

Table 1. *Consolidation and index properties.*

Parameter	Unit	C50-S50-B5		C50-S45-L5-B9	
		Curing age (days)			
		7	28	7	28
		Value			
Gs	/	2.76		2.70	
LL	%	42		62	
PI	%	15		38	
Clay Size	%	17		17	
Silt Size	%	67		73	
Sand Size	%	16		10	
C_v	cm^2/s	2.03×10^{-3}	1.24×10^{-3}	3.34×10^{-4}	3.0×10^{-3}
(q_u)	kPa	78	380	80	505

backhoe or other specific equipment excavates the trench to the desired depth. At the same time, the excavated part of the trench is prevented from collapsing by pumping a bentonite-water slurry into it and keeping the trench full of batch slurry. Throughout the trench excavation, existing bentonite-water slurry penetrates through the sidewall into adjacent sandy layers. This bentonite filter cake then leads to reduced interface shear strength between the constructed wall and surrounding soils. Lam et al. [18] provided the strength of the shear reduction factor, R, from calibrated CPTu data to be 0.1 to 0.3.

Although the model provided by Li et al. [6] proposed a better estimation for σ'_h, the σ'_v achieved by this method was considered the major principal effective stress and was greater than σ'_h. This approach is not well suited to deep trenches and may raise a question where the lateral squeezing effect is considered to be specified on the basis of Filz's [5] theory.

The development of lateral earth pressure behind a slurry wall creates inward displacement from mixture placement to consolidation completion. Laboratory investigation for increased strength of CSB also indicates that this deformation will stop to develop after 28 days of curing time because the unconfined compressive strength test values are greater than those provided by effective horizontal stress [19]. Vertical effective stress determination has various stages, starting from the at-rest condition (mixture placement) to the active condition (consolidation completion). In the analysis, the adjacent soil layer is assumed to have uniform properties with no change of layer type. The method of analysis estimates not only the progressive lateral earth pressure at each depth but also the dilatancy angle, ψ, development as $0 \le \beta \le 1$. The predicted vertical effective stress using this method is in good agreement with those provided by Ke et al. [8] and remains below effective horizontal stress at each depth. Moreover, by considering the effects of both arching and lateral squeezing, this model presents a considerable improvement of stress estimation in CSB slurry walls. The stress values obtained by the proposed model are used to estimate the permeability (k) of the cured wall with depth through changes of the void ratio. The following affiliation between stress and permeability proposed by Yeo et al. [4] is used to exemplify the potential influence for samples of this study:

$$e = 1.25 - 0.21\log\left(\frac{\sigma'(kPa)}{5}\right) \tag{20}$$

so that

$$k(m/s) = 1.5\times10^{-9}\times10^{(e-1.25)/0.22} \tag{21}$$

where σ′ and e are effective consolidation stress and void ratio, respectively. Again, the conventional thinking is that the mechanical curing set provides one-dimensional (1D) stacking in CSB examples to control the proportion of gaps in

each addition. In this way, the estimated effective stress obtained by the proposed model is adjusted by a comparable main effective pressure that would provide an inseparable fraction of the gap in the conditions of the 1D community, as indicated by Filz et al. [2]

$$\sigma^{-1} = \frac{3\sigma'_{mean}}{1+2K_b} \quad (22)$$

where σ^{-1} is the equivalent major effective stress, σ'_{mean} is the mean effective stress in cured samples, and K_b is assumed to be present as υ/ (1-υ) for the consolidation test. Li et al. [6] indicated that the mean effective stress, σ^{-1}, can be adjusted for the plain-strain problem as follows:

$$\sigma^{-1} = (1-\upsilon)\left(\sigma'_v + \sigma'_h\right) \quad (23)$$

The estimated permeability profile controlled by the proposed effective stress at each depth is given in Figures 5 and 6. In the shallow depth (z ≤ 7 m) where the arching effect is still dominant, permeability is higher than 10^{-9} m/s as a result of lower effective stress and higher void ratio. The permeability decreases slightly with depth as stress increases and reaches 1×10^{-9} m/s in the region of 17 m and remains constant down to the trench's floor for the method proposed here. Predicted permeabilities for CSB in this study (Figures 5 and 6) appear to be well substantiated by those achieved in previous studies for both laboratory and field monitoring [20, 9]. However, the permeability predicted by the geostatic method is lower than the presented method as a result of the greater stress values. According to the laboratory consolidation test results in this study, permeability decreases with depth as the void ratio decreases. Moreover, as specimens' hydration improve with increased curing times, the particles of the cementitious materials fill the void between them. Simultaneously, for the amended specimen, the presence of further bentonite content in addition to lime gave lower values than (C50-S50-B5) specimens for both curing times. The laboratory study also shows that permeability values for both mixtures at each curing period are slightly higher than those achieved by the proposed method (Figures 5 and 6). The consolidometer permeation values in soft-to-medium consistency materials are 10 to 100 times greater than those gained by the flexible wall permeation test [21, 19].

Parametric Study

The proposed physical modeling in this study considers the effects of adjacent soil and mixture properties along with trench size on the steady-state effective stress profile. The values and the impact of corresponding parameters for both surrounded soils and mixtures are provided in Table 2. The width and depth of the trench are 1.2 m and 30 m, respectively [8]. The laboratory investigation was performed to define the CSB mixture's properties and the impact of curing ages at 7 days and 28 days.

The values of subgrade modulus for granular soils *k* correspond to saturated medium dense sand and varied with depth; the modulus of the horizontal subgrade reaction is defined as n_h = 4500 kN/m^3 [13]. The impact of lateral squeezing throughout mixture consolidation and inward displacement is employed to determine σ'_h in the CSB slurry wall according to depth.

The shear strength reduction factor at the interface of the mixture-adjacent soil also vary with depth and is *R* = 0.1—0.25 according to data provided by Li et al. [6]. As β indicates the wall stage at the elastic part of the inward displacement, the intermediate values for β = 1 at z = 0 to β = 0 at z = H have been employed to determine *R*-value for each depth. Accordingly, the C'_{in} and $Ø'_{in}$ parameters of the CSB wall are a function of *R* and change with depth. The constrained modulus, *D*, for each mixture is determined on the basis of a one-dimensional consolidation test. Similarly, Young's modulus *E* values for the samples are related to *D* based on elasticity theory (see Equation 18). The impact of adjacent soils on effective vertical stress, σ'_v, is determined by using various values of $Ø'_{CSB}$. As discussed before, the minor effective stress, σ'_v, value is a function of β, $Ø'_{CSB}$, and σ'_h, and must be determined for each depth. The described solution steps, however, need a parametric study to specify the impact of wall tilt, β, on the shear strength parameters. The values, as mentioned above for each parameter, are influenced by mixture properties at each curing age.

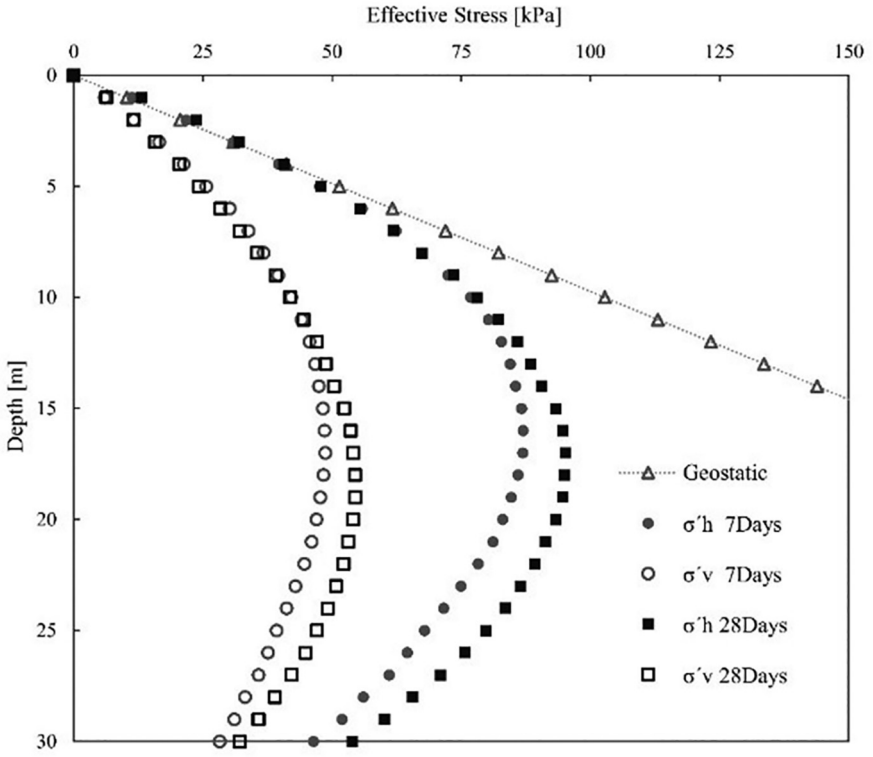

Figure 3: *Effective stress values for the C50-S50-B5 mixture.*

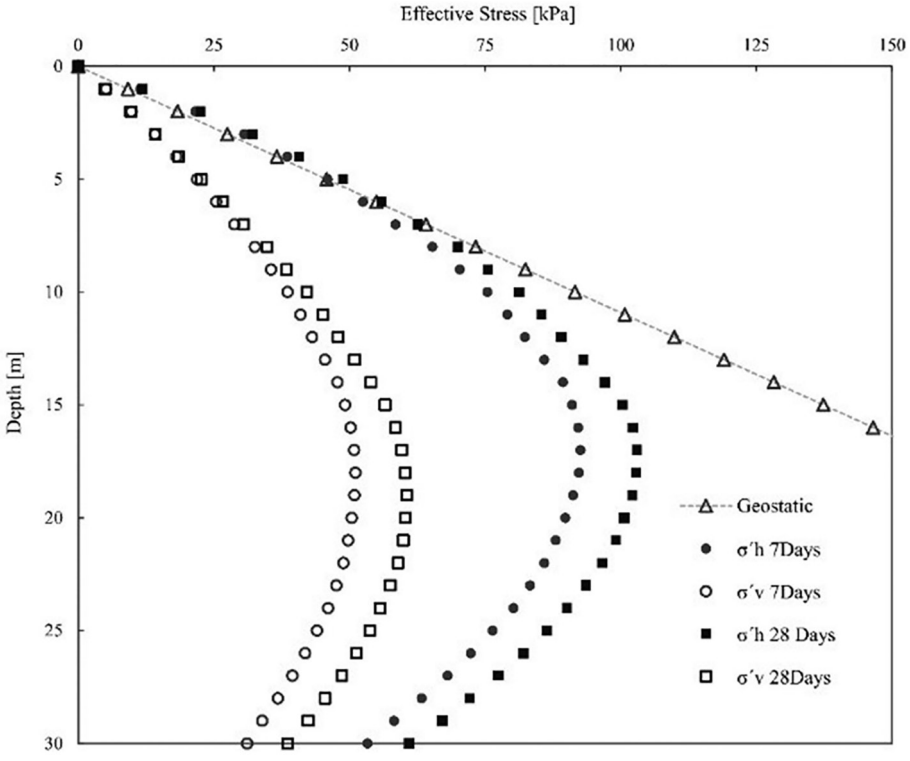

Figure 4: *Effective stress values for the C50-S45-L5-B9 mixture.*

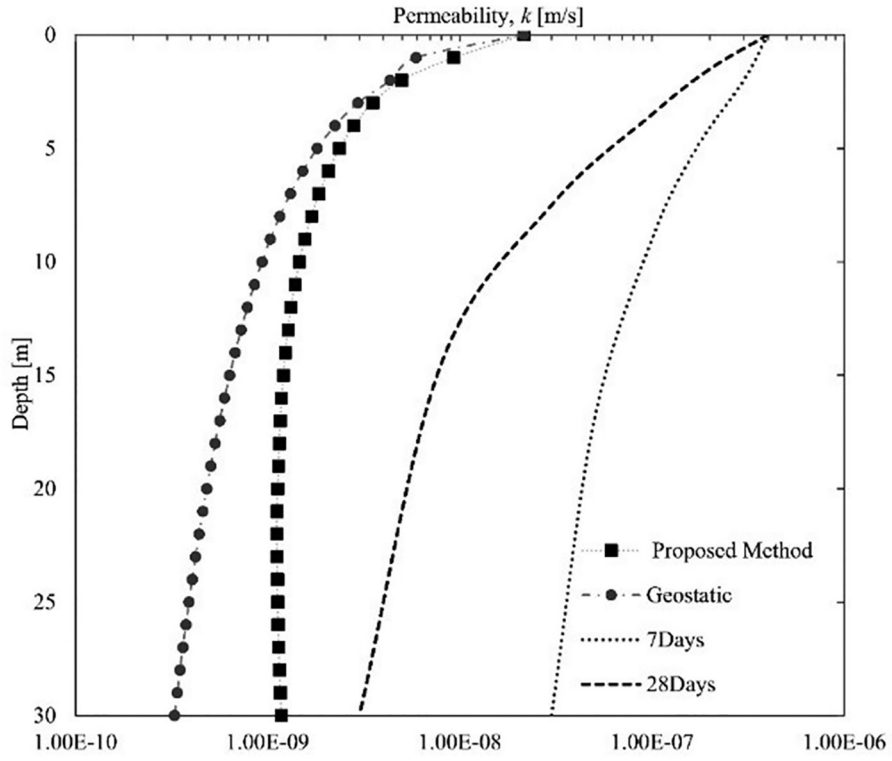

Figure 5: *Estimated permeability and laboratory test results for the C50-S50-B5 mixture.*

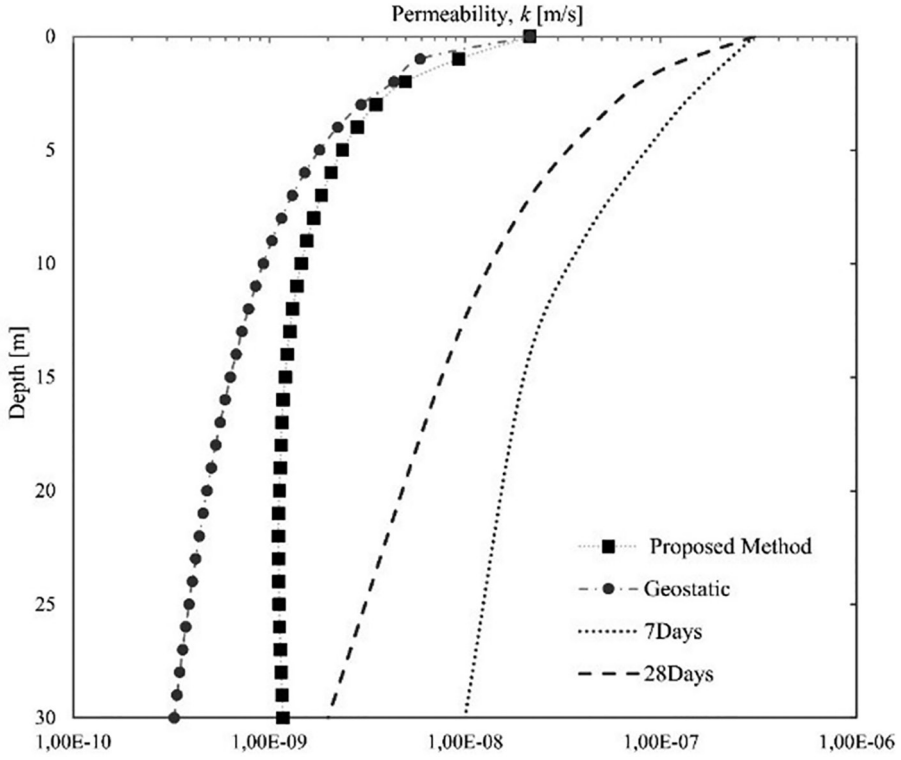

Figure 6: *Estimated permeability and laboratory test results for the C50-S45-L5-B9 mixture.*

Table 2. *Geometric and mixture properties.*

Parameter	Unit	C50-S50-B5		C50-S45-L5-B9	
		Curing age (days)			
		7	28	7	28
		Value			
B	m	1.2*			
H	m	30*			
γ'_{csb}	kN/m^3	11.9	13.8	12.3	12.6
υ	/	0.26	0.22	0.25	0.18
C'	kPa	66	133	67	160
Ø′	°	18	21	23	25
n_h	kN/m^3	4500†			
R	/	0.1—0.25‡			

*Ke, H et al. 2018.
†Das 1998.
‡Lam et al. 2014.

Discussion

In this study, the effective horizontal stress, σ'_h, reduces owing to low lateral squeezing impact as K increases linearly, and the maximum values are between 15 m to 20 m for both samples (Figures 3 and 4). The major and minor effective stress values for both samples are decreased as z > 20 m and reached lower than 62 kPa for the C50-S45-L5-B9 and 54 kPa for C-50-S50-L5 mixtures at a depth of 30 m. The parametric study also shows that the faster the hydration rate of a sample develops, the higher the effective stresses on the self-hardening walls. However, horizontal and vertical effective stress magnitude between two curing times do not exceed 10 kPa for either mixture with depth. Besides, the properties of the CSB wall depend on mixture design and bentonite content. Considering reports from previous studies, this paper reveals that cementitious properties of slurry wall materials experience up to the 25 kPa of major and minor effective stresses with depth. The laboratory tests revealed that the hydration progression of each sample has a slight influence on the proposed effective stress values to control the lateral squeezing effect. An alternative explanation might be that the increasing values of cohesion C and internal friction angle Ø of each mixture due to curing age does not have considerable impact on stress values. Measurements were taken as shear strength reduction factor R changes with depth, that is, the function of β, and gives effective stress distribution values from the at-rest to the active condition. Moreover, the constrained modulus D and Young's modulus E values of the CSB mixtures are stress dependent and increase with depth. The results show that since the differences between the maximum and minimum value of E for both mixtures at 7-day and 28-day curing ages are relatively low, it does not have a major impact on the effective stress in the wall. The coefficient of lateral earth pressure has a significant effect on the vertical effective stress prediction. Ke et al. [8] indicated that this prediction accuracy could be improved by inputting a distribution of the lateral earth pressure coefficient with depth.

Such an investigation is developed in Equation 15, and the results are based on the determination of the intermediate value of Ø and $Ø_0$ at each depth. The proposed physical model provides a relatively good estimation of the stress distribution within CSB slurry walls. The trends of both major and minor effective stress achieved by this model are in good agreement with those calculated from CPTu data sets provided by Ke et al. [8]. The proposed stresses are used to estimate the permeability of the CSB wall and compare it with those evaluated in the laboratory for the same stress profile. Estimated permeability and laboratory test

results for the C50-S50-B5 mixture and the C50-S45-L5-B9 mixture are presented in Figures 5 and 6. The permeability results of both would seem to suggest that permeability is relatively high in the shallow depth where stress is lower and it decreases as stress increases.

The use of vertical curtains in order to contain the advance of contaminating plumes towards groundwater is increasing throughout the world [19]. These are trench-shaped excavations that can reach up to tens of meters in depth and are strategically placed to contain, diverge, or encapsulate the underground contaminating flow. Simultaneously with the excavation process, the trench is filled with a mixture of bentonite and water, called bentonite mud, which has functions of geotechnical stabilization and reduced permeability [7]. After the excavation, the trench is re-ground, so that part of the introduced bentonite mud is expelled, and the remaining part tends to remain, covering the walls and the bottom of the ditch and forming a thin layer (filter cake) [2].

This thin layer, if well constituted, is mainly responsible for the reduction of the permeability of the curtain [11]. The backfill, normally constituted of the excavated material itself, can be mixed with bentonite and/or cement, in order to further reduce its permeability and increase its mechanical resistance. Geomembranes can also be applied next to the backfill to further decrease the hydraulic conductivity of the curtain [2]. Lateritic soils, in turn, cover approximately 65% of the country's territory. In general, they are characterized by a mineralogical composition dominated by quartz, Fe-Al-Mn oxides/hydroxides, and kaolinite as the predominant clay. In the field, they usually present high porosity and drainability, in profiles of alteration of great thicknesses, and are quite homogeneous. Because of its wide occurrence, lateritic soils have great potential for application in vertical curtains.

Conclusion

This paper has investigated the physical model to predict effective stresses in CSB slurry walls, and considerable progress has been made for both arching and lateral squeezing effect. Taken together, the proposed model was then employed to evaluate the influence of two different self-hardening mixtures on estimated stress profile. A bentonite filter cake prior to mixture hardening reduces the shear strength between adjacent soils and the trench wall, and the provided R, C'_{CSB}, and $Ø'_{CSB}$ values change with depth according to β tilt. The principal stress of the trench wall at $z > 7$ m is horizontal, and maximum stress values are appear at $15 \leq z \leq 20$ m. A parametric study implies that the stresses in the CSB wall are initially dominated by the arching effect at shallow depth; later at $z \geq 7$ m, stresses are caused by lateral squeezing. The effective vertical stresses are then predicted based on obtained horizontal effective stresses and the transition of the lateral earth pressure coefficient from at-rest to the active condition. The proposed stresses are used to estimate the permeability of the CSB wall and compare it with those evaluated in the laboratory for the same stress profile. The permeability results of both would seem to suggest that permeability is relatively high for the shallow depth as a result of its low-stress stage, and permeability decreases as stress increases. Finally, considerable insight has been gained with regard to an appropriate stress stage prediction in the CSB wall, in which the development is consistent with calculations from CPTu data provided by previous studies.

References

[1] Opdyke, S.M., Evans, J.C. (2005): Slag-cement-bentonite slurry walls. *Journal of Geotechnical and Geoenvironmental Engineering*, 131(6), pp. 673-681.

[2] Filz, G.M., Henry, L.B., Heslin, G.M., Davidson, R.R. (2001): Determining hydraulic conductivity of soil-bentonite using the API filter press. *Geotechnical Testing Journal*, 24(1), pp. 61-71.

[3] Evans, J. C. (1994): Hydraulic conductivity of vertical cutoff walls. In: *Hydraulic Conductivity and Waste Contaminant Transport in Soil.* Daniel, D, E, Trautwein, S.J. (eds.), ASTM International: West Conshohocken, Pennsylvania.

[4] Yeo, S.S., Shackelford, C.D., Evans, J.C. (2005): Consolidation and hydraulic conductivity of nine model soil-bentonite backfills. *Journal of*

Geotechnical and Geoenvironmental Engineering, 131(10), pp. 1189-1198.

[5] Filz, G.M., 1996. Consolidation stresses in soil-bentonite backfilled trenches. In: *Environmental Geotechnics*, Kamon, M. (ed.). CRC Press: Boca Raton, Florida, pp. 497-502.

[6] Li, Y.C., Cleall, P.J., Wen, Y.D., Chen, Y.M., Pan, Q. (2015): Stresses in soil–bentonite slurry trench cut-off walls. *Géotechnique*, 65(10), pp. 843-850.

[7] Ruffing, D.G., Evans, J.C., Malusis, M.A. (2010): Prediction of earth pressures in soil-bentonite cutoff walls. In: *GeoFlorida 2010: Advances in Analysis, Modeling & Design,* Fratta, D.O., Pupala, A.J., Muhunthan, B. (eds), ASCE Library: Reston, Virginia, pp. 2416-2425.

[8] Ke, H., Tong, X., Li, Y.C., Chen, Y.M., Wen, Y.D. (2018): Force equilibrium–based model for predicting stresses in soil-bentonite cutoff walls. *Journal of Geotechnical and Geoenvironmental Engineering*, 144(2), p.04017112.

[9] Ruffing, D. G., Evans, J.C. (2014): Case study: construction and in situ hydraulic conductivity evaluation of a deep soil-cement-bentonite cutoff wall. In: *Geo-Congress 2014: Geo-Characterization and Modeling for Sustainability,* Abu-Farsakh, M., Yu, X., Hoyos, L.R. (eds.), ASCE Library: Reston, Virginia, pp. 1836-1848.

[10] Bang, S., Kim, H.T. (1986): At rest to active earth pressure transition. *Transportation Research Record*, 1105, pp. 41-47.

[11] Evans, J.C., Fang, H.Y., Kugelman, I.J. (1985): Containment of hazardous materials with soil-bentonite slurry walls. In: *Proceedings of the 6th National Conference on the Management of Uncontrolled Hazardous Waste Sites,* United States Environmental Protection Agency: Silver Spring, Maryland, pp. 249-252.

[12] Potyondy, J.G. (1961): Skin friction between various soils and construction materials. *Geotechnique*, 11(4), pp. 339-353.

[13] Das, B.M. (1998): *Principles of Foundation Engineering*. Brooks/Cole: Pacific Grove, California.

[14] Clough, G.W., Duncan, J.M. (1991): Earth pressures. In: *Foundation Engineering Handbook*, Fang H.Y. (ed.). Springer Science–Business Media: New York.

[15] Nejad, B.G., Osborne, T., Carter, J.P. (2017): Forensic Investigation of a Slurry Wall Failure: A Case Study. In: *Grouting*, ASCE Library: Reston, VA, USA, pp. 513-522.

[16] Sridharan, A., Nagaraj, H.B. (2004): Coefficient of consolidation and its correlation with index properties of remolded soils. *Geotechnical Testing Journal,* 27, 469-474.

[17] Rao, D.K., Raju, R.P. & Kumar, R.A. (2011): Consolidation characteristics of treated marine clay for foundation bed soils. *International Journal of Engineering Science and Technology*. 3(2), pp. 788-796.

[18] Lam, C., Jefferis, S.A., Martin, C.M. (2014): Effects of polymer and bentonite support fluids on concrete–sand interface shear strength. *Géotechnique*, 64(1), pp. 28-39.

[19] Talefirouz, D., Cokça, E., Omer, J. (2016): Use of granulated blast furnace slag and lime in cement-bentonite slurry wall construction. *International Journal of Geotechnical Engineering*, 10(1), pp. 81-85.

[20] Boscardin, M., Patterson, C., Landis, M., Younan, J. C., Aghjayan, D, (2006): Evaluation of permeability of containment slurry walls. In: GeoCongress 2006: *Geotechnical Engineering in the Information Technology Age,* DeGroot, D., DeJong, J., Frost, D., Baise, L. (eds.). American Society of Civil Engineers: Reston, Virginia, pp. 1-6.

[21] Oweis, I.S., Khera, R.P. (1990): *Geotechnology of Waste Management*. Butterworth-Heineman: Oxford, UK.

Original Scientific Article • DOI: 10.2478/rmzmag-2021-0009

Received: August 03, 2021
Accepted: November 24, 2021

Field Observations, Petrography, and Microstructures of Granite from Abeokuta Southwestern Nigeria

Terenska opažanja, petrografija in mikrostrukture granita iz Abeokuta v jugozahodni Nigeriji

Ehitua Julius Oziegbe*, Olusegun Abimbola Aribike
Department of Geosciences, University of Lagos, Lagos, Nigeria
*Corresponding author: E-mail: eoziegbe@unilag.edu.ng

Abstract in English

The granite of Abeokuta is part of the Older Granite suite of the basement complex of southwestern Nigeria. Field observation has identified the granite as porphyritic in texture, with a preferred alignment of megacrysts of K-feldspar >5 cm that are mostly euhedral to subhedral in shape. K-feldspar megacrysts are predominantly yellowish, but whitish and pinkish colouration has also been observed. The dark grey porphyritic, mafic rock composition occurs as enclaves within the granite, with phenocrysts having a preferred alignment as the enclosing granite. Also, K-feldspar megacrysts show zoning defined by concentric arrangement of inclusions of biotite relative to the crystal faces. Petrographic study shows the following minerals in order of abundance: K-feldspar, biotite, quartz, and plagioclase, with K-feldspar having a microperthitic intergrowth and biotite crystals aligned in a preferred direction. Evidence such as the crystal shape of K-feldspars, preferred alignment of K-feldspar phenocrysts, and concentric crystallographic arrangements of inclusions of biotite in K-feldspar support a magmatic/phenocrystic origin of K-feldspar megacrysts of Abeokuta granite rather than originating by growing in a solid state as porphyroblasts.

Keywords: megacrysts, microperthitic, K-feldspar, zoning, porphyroblasts

Abstract in Povzetek

Abeokutski granit pripada Starejšemu granitu Bazalnega kompleksa v jugozahodni Nigeriji. Glede na terenska opažanja ima granit porfirsko strukturo. Več kot 5 cm veliki evhedralni do subhedralni vtrošniki kalijevih glinencev kažejo usmerjenost. Vtrošniki kalijevih glinencev so večinoma rumenkasto obarvani, čeprav so prisotni tudi beli do rožnati kristali. V granitu se pojavljajo vključki temno sive porfirske mafične kamnine, ki vsebuje fenokristale z enako orientacijo kot jo imajo kristali kalijevih glinencev v okolnem granitu. Vtrošniki kalijevih glinencev nadalje kažejo conarno zgradbo, ki jo določa koncentrična razporeditev vključkov biotita. S petrografsko preiskavo so bili določeni naslednji minerali, našteti od najpogostejših do najbolj redkih: kalijevi glinenci, biotit, kremen in plagioklazi. Kalijevi glinenci imajo mikropertitsko preraščanje. Kristali biotita so med seboj enako usmerjeni. Oblika kristalov kalijevih glinencev, preferenčna orientacija fenokristalov kalijevih glinencev in koncentrična razporeditev vključkov biotita v kalijevih glinencih so nekatere lastnosti, ki podpirajo magmatski/porfirski izvor vtrošnikov kalijevega glinenca v Abeokutskem granitu in ne porfiroblastično rast iz trdnih raztopin.

Ključnebesede: vtrošniki, mikropertit, kalijev glinenec, conarna rast, porfiroblasti

Introduction

Granite is the most abundant rock in the continental crust. A-type granite is proposed to originate from the fractional crystallization of the upper mantle [1–6]. Abeokuta, the study area, shares a boundary with the sedimentary rocks of the Dahomey Basin. Large crystals of K-feldspar with the preferred alignment typifies the granite of Abeokuta (Figure 1). Arguments have been put forward to suggest the origination of these megacrysts in granite. In some of the literature, it is agreed that phenocrysts are formed through early growth by crystallization from the molten portion of magma [7–11], while the later developing porphyroblasts arise from a water-rich fluid phase usually in the subsolidus environment [12–16]. The current study uses field observations and petrographic features to determine the origin of K-feldspar megacrysts in the granite of Abeokuta.

Geological Setting

Nigeria is located within the section of Pan-African reactivation 600 + 150 Ma [17, 18] to the east of the West African craton. The older granite suite of Nigeria comprises for the most part tonalitic to granitic calc-alkaline intrusions which were emplaced at a period of about 800–500 Ma ago [19–22]. The Older Granite suite of Nigeria has been described as a high-level, I-type intrusion [23–25]. The phrase 'Older Granite' was coined by Falconer [26] to separate the deep-seated, often concordant granites of the Precambrian basement complex of Nigeria from the highly discordant tin-bearing granite which is found in Northern Nigeria. Older Granite is one of the substantial rock units identified in the Precambrian basement complex of Nigeria [27]. Older Granite suites have a wide range of composition that varies

Figure 1: *a) Field photograph showing dispersed K-feldspar megacrysts with the preferred alignment from Abeokuta. Megacryts are subhedral to euhedral b) Hand specimen sample of porphyritic granite from Abeokuta showing a large phenocryst of K-feldspar in a matrix of biotite.*

Figure 2: *Field photograph showing a xenolith of porphyritic mafic rock within a felsic, porphyritic granite.*

from granite through granodiorite, adamellite/quartz monzonite to syenite [27]. The granitic rock of Abeokuta is porphyritic in texture, with phenocrysts of K-feldspar aligned in the preferred direction and thus defining foliation (Figure 1a). Where aligned, the phenocrysts trend in a NW-SE direction on the field. There are quatzo-feldspathic veins and pegmatitic veins of different dimensions running through the granite. Xenoliths of porphyritic mafic rock composition exist within the main porphyritic granite (Figure 2). The sizes of phenocrysts observed on the field vary from a few millimeters to about 10.5 cm in length (Figure 3a).

Granite has a greater amount of K-feldspar megacrysts (Figure 3a and 3b) as compared to matrix and can be described as megacryst-dominated. Some K-feldspar megacrysts are zoned (Figures 3c–3h), with inclusions of biotite-defining zonation. The inclusions of biotite are arranged in a concentric pattern along the crystal faces of the zoned megacrysts (Figures 3c, 3e, and 3f). K-feldspar megacrysts vary in colour from yellowish, whitish, and in some cases pinkish colouration. The associated mafic porphyritic rock component also shows zoned crystals of K-feldspars (Figures 3g and 3h). The mafic rock components, which occur as enclaves within the porphyritic granite, have micro-phenocrysts aligned in the same direction as the megacrysts in the porphyritic granite (Figure 4).

Materials and methods

Thin sections of porphyritic granite were prepared at the Department of Geology, Obafemi Awolowo University in Ife, Nigeria. The petrographic study was carried out at the Department of Geosciences, University of Lagos using a polarizing microscope, and optical properties of the minerals were studied under both plane-polarized light (PPL) and cross-polarized light (XPL).

Results

Petrography

The granite comprises the following minerals in order of abundance: K-feldspar, biotite, quartz, and plagioclase with apatite occurring as an accessory mineral. The crystals of K-feldspar are subhedral to anhedral in shape and occur as phenocrysts in a matrix of quartz and biotite (Figure 5). K-feldspar is poikilitic, having inclusions of biotite (Figure 5a). A cross-hatched twinning is an indication of the presence of microcline, a type of K-feldspar (Figure 5b). The plagioclase feldspar has polysynthetic twinning, also referred to as albite twinning (Figure 5c). Plagioclase shows a high level of albitization (Figure 5c). K-feldspar exhibits perthitic texture (Figures 5d and 5e). Quartz crystals occur as inclusions in phenocrysts of K-feldspar (Figure 5e), and exhibit a symplectic texture between K-feldspar and plagioclase (Figure 5f). Biotite has crystals with a preferred alignment (Figures 5g and 5h).

Discussion

Megacryst K-feldspars are prominent features in Abeokuta granite. For growth of crystals, essential components in the magma must diffuse through the melt to the crystal-melt interface, and also excess or excluded components need to diffuse away from the interface. It has been shown that diffusivities in silicate melts usually reduce in the sequence Na ≥ K > Ca > Al >> Si [28, 29]. Therefore, the rate-limiting event necessary for the crystallization of feldspars and quartz is the attainment of the correct percentages of Si:Al available at the crystal-melt margins. To this end, the megacrystic nature of K-feldspars means that the composition of K-feldspar is highly similar to that of the granitic liquid in terms of the major components that diffuse slowly in silicate melts. Other granite-forming minerals do not share this compositional similarity with the granitic liquid. The time at which K-feldspar starts to crystallize also depends on the bulk chemical composition of the magma. More alkalic magmas will naturally precipitate K-feldspar earlier than those of less-K-rich compositions [30]. Difficulty in the nucleation of K-feldspar has been given as the reason why K-feldspar forms megacrysts; once nucleation commences, it grows rapidly, thus a small number of very large crystals is formed [31]. The phenocrysts of the K-feldspars can be termed megacrysts

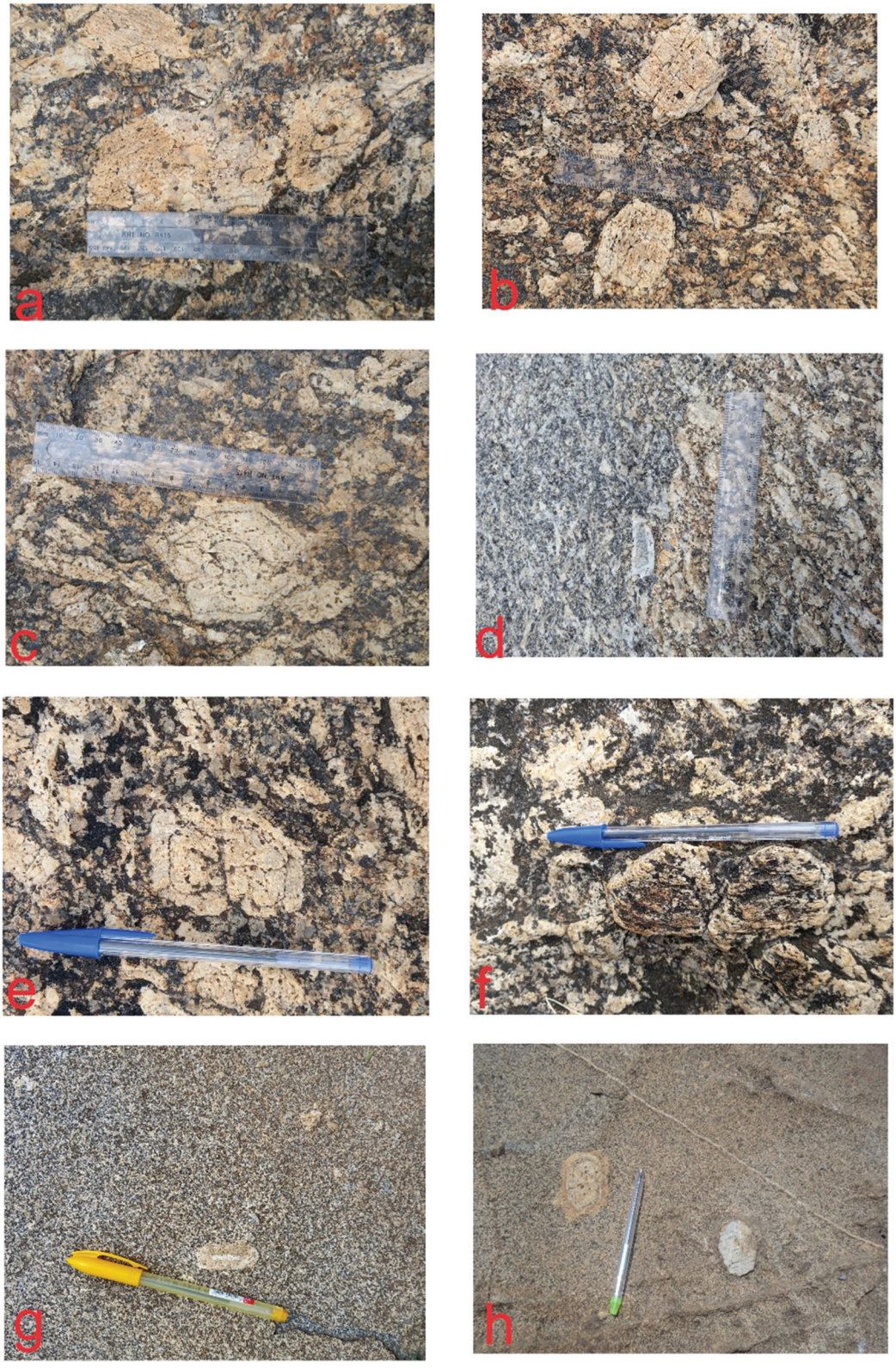

Figure 3: *Field photographs showing: a) megacrysts of K-feldspar, b) subhedral-euhedral megacrysts of K-feldspar, c) zoned crystals with concentric inclusions of biotite, d) zoned crystals of K-feldspar with a core rich in biotite inclusion, e) K-feldspar magacrysts with inclusions of biotite-defining zonation, f) Zoned K-feldspar crystal with inclusions of biotite, g) zoned crystal of K-feldspar in porphyritic mafic rock, h) matrix-dominated porphyritic mafic rock with zoned megacrysts of K-feldspar.*

Figure 4: *Field photograph showing enclaves of a pophyritic mafic rock component within porphyritic granite. The micro-phenocrysts, megaphenocrysts, and biotite crystals are all aligned in the same direction.*

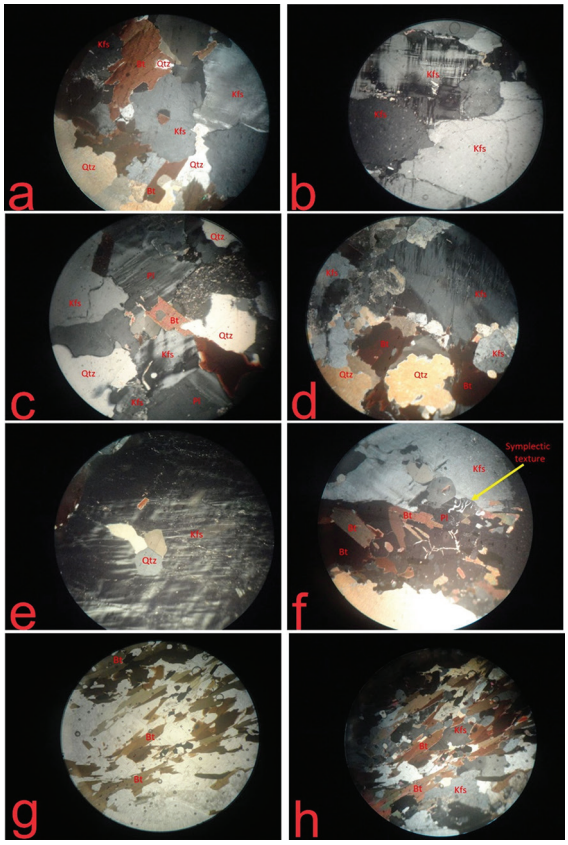

Figure 5: *Photomicrographs of porphyritic granite showing a) inclusions of biotite in K-feldspar (Kfs), XPL b) tartan twining in K-feldspar (Kfs), XPL c) albitization of plagioclase feldspar (Kfs), XPL d) perthitic texture in K-feldspar (Kfs), XPL e) K-feldspar with perthitic intergrowth and inclusions of quartz (Qtz), XPL f) symplectic texture between K-feldspar and plagioclase (Pl), XPL g) biotite (Bt) crystals with a preferred alignment, PPL h) biotite (Bt) and K-feldspar (Kfs) in close association, XPL.*

on the basis of their size, which is several times larger than the plagioclase. This might be due to the low rate of nucleation and the rapid growth rate [9, 32]. However, Moore and Sisson [33] have proposed that K-feldspar grows into larger megacrysts than other minerals in granite because of the similarities in the composition of K-feldspar and the granitic components that diffuse slowly in silicate melts. In most zones, a preferred alignment of the K-feldspar megacrysts forms (Figure 1a), defining foliation. Foliated granite has been reported in the members of the Older Granite suite in other parts of the Basement Complex of Nigeria [34, 35, 19, 36]. These foliations in granitoids can form through magmatic flow [37, 38]. The preferred alignment of crystals suggests that the magma attained a high viscosity and could have occurred in the later stage of crystallization for the preferred orientation to be preserved [39]. Zoning is a common feature in the K-feldspar megacrysts (Figures 3c–3h). Dark inclusions of biotite are displayed in internal zones aligned to the outer margins of megacrysts (Figures 3c and 3e). A number of igneous microtextural features, such as simple twinning and concentric arrangements of inclusions, are typical of K-feldspar megacryst of magmatic origin [8, 40, 41]. Microgranite enclaves have also been (Figure 4) derived, which implies that the megacrysts moved as independent crystals suspended in liquid, and therefore did not develop in situ [42]. The elongation of such microgranitoid enclaves (Figure 4), without the presence of plastic contortion of the minerals provides evidence of magmatic flow [38, 43]. The inclusions within the megacrysts are far smaller than their matrix equivalents, and thus show characteristics specific to magmatic growth, which includes zonal alignment (Figures 3c and 3f) and euhedral shape [8]. K-feldspar megacrysts have been interpreted to be early crystallizing phases [16]. Symplectic intergrowth between K-feldspar and plagioclase can be observed in thin section (Figure 5f), which provides us with a clue about the final crystallization process in the granite under study. Symplectic texture has been reported in granitoids from southwestern Nigeria [44]. Symplectic texture in petrology is characterized by the intergrowth of two minerals that crystallized simultaneously [45].

Symplectic intergrowth in granite has been described by different authors across continents [46, 47]. Replacement of plagioclase by K-feldspar (Figure 5c), as described by Collins [48], appears to be a very common phenomenon. Replacement of plagioclase by K-feldspar at low temperatures has been reported [49], but a high temperature alteration of plagioclase to K-feldspar is also possible [49, 50]. For instance, at a temperature of about 25–350°C, plagioclase feldspars are altered to sericite through weathering [51]. Some of the quartz crystals exhibit a wavy form of extinction. There are minor fractures on some K-feldspar megacrysts (Figure 3c) and micro-fractures on K-feldspar crystals (Figure 5b), which are evidences of deformation. The fact that biotite occurs as inclusions in the K-feldspar follows the Bowen reaction series in which the biotite crystalizes first at a higher temperature before the K-feldspar crystalizes at a much lower temperature (Figure 5a). The K-feldspar has many of the other minerals in the rock present as inclusions, which is an indication of the late-stage crystallization of K-feldspar [8]. The alkali feldspar shows flame perthitic to mesoperthitic structure (Figures 5d and 5e). The formation of perthite has been explained to be a replacement-type reaction (Na-K exchange) that takes place between K-feldspar and plagioclase in an environment of low-moderate differential stress usually accompanying rapid cooling [52–56]. The presence of exsolution lamellae (Figures 5d and 5e) could be found in recrystallized K-feldspar formed at hypersolvus temperatures [37, 57]. Several researchers have used microtextures, such as perthite and myrmekite, as tools to investigate the cooling mechanism of rocks [58–61], which can also be linked to exsolution and hydrothermal subsolidus activity.

Conclusion

Observations such as the crystal shape of K-feldspars and concentric crystallographic arrangements of inclusions of biotite in K-feldspar have provided evidence supporting a magmatic/phenocrystic origin for K-feldspar megacrysts in Abeokuta granite rather than originating while growing in a solid state as in the formation of porphyroblasts. K-feldspar's inclusion of other minerals and the preferred alignment of K-feldspar magacrysts attributed to magmatic flow suggest late crystallization of K-feldspar.

References

[1] Turner, S.P., Foden, J.D., Morrison, R.S. (1992): Derivation of some A-type magmas by fractionation of basaltic magma: an example from the Padthaway Ridge, South Australia. *Lithos,* 28(2), pp. 151–179. Doi.org/10.1016/0024-4937(92)90029-X

[2] Atherton, M.P. (1993): Granite magmatism. *Journal of the Geological Society*, 150(6), pp. 1009–1023. Doi.org/10.1144/gsjgs.150.6.1009

[3] Soesoo, A. (2000): Fractional crystallization of mantle-derived melts as a mechanism for some I-type granite petrogenesis: an example from Lachlan Fold Belt, Australia. *Journal of the Geological Society*, 157(1), pp. 135–149. Doi.org/10.1144/jgs.157.1.135

[4] Jarrar, G.H., Manton, W.I., Stern, R.J., Zachmann, D. (2008): Late Neoproterozoic A-type granites in the northernmost Arabian-Nubian Shield formed by fractionation of basaltic melts. *Geochemistry*, 68(3), pp. 295–312. Doi.org/10.1016/j.chemer.2006.09.002

[5] Namur, O., Charlier, B., Toplis, M.J., Higgins, M.D., Hounsell, V., Liégeois, J.P., Vander Auwera, J. (2011): Differentiation of tholeiitic basalt to A-type granite in the Sept Iles layered intrusion, Canada. *Journal of Petrology*, 52(3), pp. 487–539. Doi.org/10.1093/petrology/egq088

[6] Zhou, G., Wu, Y., Wang, H., Qin, Z., Zhang, W., Zheng, J., Yang, S. (2017): Petrogenesis of the Huashanguan A-type granite complex and its implications for the early evolution of the Yangtze Block. *Precambrian Research*, 292, pp. 57–74. DOI.org/10.1016/j.precamres.2017.02.005

[7] Kerrick, D.M. (1969): K-feldspar megacrysts from a porphyritic quartz monzonite central Sierra Nevada, California. *American Mineralogist: Journal of Earth and Planetary Materials*, 54(5–6), pp. 839–848.

[8] Vernon, R.H. (1986): K-feldspar megacrysts in granites—phenocrysts, not porphyroblasts. *Earth-Science Reviews*, 23(1), pp. 1–63. Doi.org/10.1016/0012-8252(86)90003-6

[9] Cox, R.A., Dempster, T.J., Bell, B.R., Rogers, G. (1996). Crystallization of the Shap Granite: Evidence from zoned K-feldspar megacrysts. *Journal of the Geological*

Society, 153(4), pp. 625–635. Doi.org/10.1144/gsjgs.153.4.0625

[10] Johnson, B.R., Glazner, A.F. (2010): Formation of K-feldspar megacrysts in granodioritic plutons by thermal cycling and late-stage textural coarsening. *Contributions to Mineralogy and Petrology*, 159(5), pp. 599–619. Doi.org/10.1007/s00410-009-0444-z

[11] Winter, J.D. (2001): *An Introduction to Igneous and Metamorphic Petrology*. Prentice Hall, Upper Saddle River, New Jersey, 699 pp.

[12] Oyawoye, M.O. (1962): The petrology of the district around Bauchi, Northern Nigeria. *The Journal of Geology*, 70(5), pp. 604–615. Doi/abs/10.1086/626855

[13] Oyawoye, M.O. (1967): The petrology of a potassic syenite and its associated biotite pyroxenite at Shaki, Western Nigeria. *Contributions to Mineralogy and Petrology*, 16(2), pp. 115–138.

[14] Dickson, F.W., Sabine, C.P. (1967): Barium zoned large K-feldspars in quartz monzonites of eastern and southeastern California [abs]. *Geological Society of America Special Paper*, 115, p. 323.

[15] Oyawoye, M.O. (1972): The basement complex of Nigeria. *African Geology*, I. Ibadan University Press, Ibadan , pp. 67–99.

[16] Johnson, B.R., Glazner, A.F., Coleman, D.S. (2006): Significance of K-feldspar megacryst size and distribution in the Tuolumne Intrusive Suite, California [abs.]. In: *102nd Annual Meeting of the Cordilleran Section, Geological Society of America: Abstracts with Programs;* Vol. 38, No. 5, p. 93.

[17] Kennedy, W.Q. (1964): The structural differentiation of Africa in the Pan-African (+/-500 my) tectonic episode. *University of Leeds, Research Institute of African Geology, Annual Report on Scientific Results*; 8, pp. 48–49.

[18] Clifford, T.N. (1970): The Structural Framework of Africa. In: *African Magmatism and Tectonics*. Clifford, T.N., Gass, I.G. (eds.). Oliver and Boyd: Edinburgh, pp. 1–26.

[19] Van Breemen, O., Pidgeon, R.T., Bowden, P. (1977): Age and isotopic studies of some Pan-African granites from North-central Nigeria. *Precambrian Research*, 4(4), pp. 307–319. Doi.org/10.1016/0301-9268(77)90001-8

[20] Ogezi, A.E.O. (1977): *Geochemistry and geochronology of basement rocks from northwestern Nigeria.* Ph. D. Thesis. University of Leeds, Department of Earth Sciences: Leeds, 298 pp.

[21] Grant, N.K. (1978): Structural distinction between a metasedimentary cover and an underlying basement in the 600-my-old Pan-African domain of northwestern Nigeria, West Africa. *Geological Society of America Bulletin*, 89(1), pp. 50–58. Doi.org/10.1130/0016-7606(1978)89%3C50:SDBAMC%3E2.0.CO;2

[22] Cahen, L., Snelling, N.J., Delhal, J., Vail, J.R., Bonhomme, M., Ledent, D. (1984): The West African Craton: The Guinea Rise. In: *The Geochronology and Evo1ution of Africa,* Cahen L., Snelling N.J., Delhal J., Vail J.R., et al. (eds.). Clarendon Press,;z Oxford, UK, pp. 296–311.

[23] Chappell, B.W. (1974): Two contrasting granite types. *Pacific Geology*, 8, pp. 173–174.

[24] Pitcher, W.S. (1979a): The nature, ascent and emplacement of granitic magmas. *Journal of the Geological Society*, 136(6), pp. 627–662. Doi.org/10.1144/gsjgs.136.6.0627

[25] [Pitcher, W.S. (1979b): Comments on the geological environments of granites. In: *Origin of Granite Batholiths Geochemical Evidence*, Atherton, M.P., Tarneyh, J. (eds.). Birkhäuser: Boston, pp. 1–8. Doi.org/10.1007/978-1-4684-0570-5_1

[26] Falconer, J.D. (1911): *The Geology and Geography of Northern Nigeria.* MacMillan: London, 295 pp.

[27] Rahaman, M.A. (1976): Review of the basement geology of Southwestern Nigeria. In: *Geology of Nigeria*, Kogbe, C.A. (ed.), Elizabethan Publishing Company: Lagos, pp. 41–58.

[28] Hofmann, A.W. (1980): Diffusion in natural silicate melts: A critical review. *Physics of Magmatic Processes*, Hargraves, R.B. (ed.). Princeton University Press: Princeton, New Jersey, pp. 385–417.

[29] Hofmann, A.W., Hargraves, R.B. (2014): Diffusion in natural silicate melts: a critical review. In: *Physics of Magmatic Processes*, Hargraves, R.B. (ed.). Princeton University Press: Princeton, New Jersey, pp. 385–418. Doi.org/10.1515/9781400854493.385

[30] Williams, H., Turner, F.J., Gilbert, C.M. (1982): *Petrography: An Introduction to the Study of Rocks in Thin Section*. W. H. Freeman: San Francisco & Oxford, 626 pp.

[31] Swanson, S.E. (1977): Relation of nucleation and crystal-growth rate to the development of granitic textures. *American Mineralogist*, *62*(9–10), pp. 966–978.

[32] Paterson, S.R., Vernon, R.H., Zak, J. (2005): Mechanical instabilities and physical accumulation of K-feldspar megacrysts in granitic magma, Tuolumne Batholith, California, USA. *The Journal of the Virtual Explorer*, 18, pp. 1–18. Doi.org/10.3809/jvirtex.2005.00114

[33] Moore, J.G., Sisson, T.W. (2008): Igneous phenocrystic origin of K-feldspar megacrysts in granitic rocks

from the Sierra Nevada batholith. *Geosphere*, 4(2), pp. 387–400. Doi.org/10.1130/GES00146.1

[34] Trustwell, J.F., Cope, R.N. (1963): The Geology of Parts of Niger and Zaria Provinces. *Northern Nigeria GSN Bulletin*, 29, 53pp.

[35] Oyawoye, M.O. (1964): The geology of the Nigerian Basement Complex—a survey of our present knowledge of them. *Journal of Mining Geology and Metal*, 1(2), pp. 87–103.

[36] Tubosun, I.A., Lancelot, J.R., Rahaman, M.A., Ocan, O. (1984): U-Pb Pan-African ages of two charnockite-granite associations from south-western Nigeria. *Contributions to Mineralogy and Petrology*, 88(1), pp. 188–195. Doi.org/10.1007/BF00371422

[37] Paterson, S.R., Vernon, R.H., Tobisch, O.T. (1989): A review of criteria for the identification of magmatic and tectonic foliations in granitoids. *Journal of Structural Geology*, 11(3), pp. 349–363. Doi.org/10.1016/0191-8141(89)90074-6

[38] Vernon, R.H. (2000): Review of microstructural evidence of magmatic and solid-state flow. *Visual Geosciences*, 5(2), pp. 1–23. Doi.org/10.1007/s10069-000-0002-3

[39] Paterson, S.R., Fowler Jr, T.K., Schmidt, K.L., Yoshinobu, A.S., Yuan, E.S., Miller, R.B. (1998): Interpreting magmatic fabric patterns in plutons. *Lithos*, 44(1–2), pp. 53–82. Doi.org/10.1016/S0024-4937(98)00022-X

[40] Vernon, R.H. (1999): Quartz and feldspar microstructures in metamorphic rocks. *Canadian Mineralogist*, 37(2), pp. 513–524.

[41] Vernon, R.H. (2004): *A Practical Guide to Rock Microstructure*. Cambridge University Press: Cambridge, UK, 440 pp.

[42] Vernon, R.H., Paterson, S.R. (2008): How late are K-feldspar megacrysts in granites? *Lithos*, 104(1–4), pp. 327–336. Doi.org/10.1016/j.lithos.2008.01.001

[43] Tobisch, O.T., McNulty, B.A., Vernon, R.H. (1997): Microgranitoid enclave swarms in granitic plutons, central Sierra Nevada, California. *Lithos*, 40(2–4), pp. 321–339. Doi.org/10.1016/S0024-4937(97)00004-2

[44] Oziegbe, E.J., Ocan, O.O., Adebisi, A.P. (2020): Petrography and Microtextural Characteristics of Granodiorite from Wasimi, Southwestern Nigeria. *Earth Sciences Malaysia (ESMY)*, 4(2), pp. 82–89. Doi.org/10.26480/esmy.02.2020.51.58

[45] Allaby, M. (2013): *A Dictionary of Geology and Earth Sciences, 4th edition*. Oxford University Press: Oxford, UK, 660 pp.

[46] Pandit, D. (2015): Geochemistry of feldspar intergrowth microtextures from paleoproterozoic granitoids in Central India: implications to exsolution processes in granitic system. *Journal of the Geological Society of India*, 85(2), pp. 163–182. Doi.org/10.1007/s12594-015-0204-9

[47] Abart, R., Heuser, D., Habler, G. (2014): Mechanisms of myrmekite formation: case study from the Weinsberg granite, Moldanubian zone, Upper Austria. *Contributions to Mineralogy and Petrology*, 168(5), p. 1074. Doi.org/10.1007/s00410-014-1074-7

[48] Collins, L.G. (2003): Transition from magmatic to K-metasomatic processes in granodiorites and Pyramid Peak granite, Fallen Leaf Lake 15-Minute Quadrangle, California, USA. *Myrmekite and Metasomatic Granite*, ISSN 1526-5757, Internet publication, no. 48.

[49] Morad, S., El-Ghali, M.A.K., Caja, M.A., Sirat, M., Al-Ramadan, K., Mansurbeg, H. (2010): Hydrothermal alteration of plagioclase in granitic rocks from Proterozoic basement of SE Sweden. *Geological Journal,* 45, pp. 105–116. Doi.org/10.1002/gj.1178

[50] Cox, K.G. (2013): *The Interpretation of Igneous Rocks*. Springer Science & Business Media: New York, 450 pp.

[51] Collins, L.G., Collins, B.J. (2013): Origin of myrmekite as it relates to K-, Na-, and Ca-metasomatism and the metasomatic origin of some granite masses where myrmekite occurs. *Contribbutions to Mineralalogy and Petrology*, 213, pp. 123–156.

[52] Yund, R.A., McLaren, A.C. and Hobbs, B.E. (1974): Coarsening kinetics of the exsolution microstructure in alkali feldspar. *Contributions to Mineralogy and Petrology*, 48(1), pp. 45–55. Doi.org/10.1007/BF00399109

[53] Yuguchi, T., Nishiyama, T. (2008): The mechanism of myrmekite formation deduced from steady-diffusion modeling based on petrography: Case study of the Okueyama granitic body, Kyushu, Japan. *Lithos*, 106(3–4), pp. 237–260. Doi.org/10.1016/j.lithos.2008.07.017

[54] Parsons, I., Lee, M.R. (2009): Mutual replacement reactions in alkali feldspars I: microtextures and mechanisms. *Contributions to Mineralogy and Petrology*, 157(5), pp. 641–661. Doi.org/10.1007/s00410-008-0355-4

[55] Parsons, I., Magee, C.W., Allen, C.M., Shelley, J.M.G., Lee, M.R. (2009): Mutual replacement reactions in

alkali feldspars II: trace element partitioning and geothermometry. *Contributions to Mineralogy and Petrology*, 157(5), pp. 663–687. Doi.org/10.1007/s00410-008-0358-1

[56] Parsons, I., Gerald, J.D.F., Lee, J.K., Ivanic, T., Golla-Schindler, U. (2010): Time–temperature evolution of microtextures and contained fluids in a plutonic alkali feldspar during heating. *Contributions to Mineralogy and Petrology*, 160(2), pp. 155–180. Doi.org/10.1007/s00410-009-0471-9

[57] Vernon, R.H., Williams, V.A., D'arcy, W.F. (1983): Grain-size reduction and foliation development in a deformed granitoid batholith. *Tectonophysics*, 92(1–3), pp. 123–145. Doi.org/10.1016/0040-1951(83)90087-2

[58] Harlov, D.E., Wirth, R. (2000): K-feldspar–quartz and K-feldspar–plagioclase phase boundary interactions in garnet–orthopyroxene gneiss's from the Val Strona di Omegna, Ivrea–Verbano Zone, northern Italy. *Contributions to Mineralogy and Petrology*, 140(2), pp. 148–162. Doi.org/10.1007/s004100000185

[59] Yuguchi, T., Nishiyama, T. (2007): Cooling process of a granitic body deduced from the extents of exsolution and deuteric sub-solidus reactions: Case study of the Okueyama granitic body, Kyushu, Japan. *Lithos*, 97(3–4), pp. 395–421. Doi.org/10.1016/j.lithos.2007.01.005

[60] Nanda, J., Gupta, S., Mamtani, M.A. (2009): Analysis of deformation fabric in an alkaline complex (Koraput): Implications for time relationship between emplacement, fabric development and regional tectonics. *Journal of the Geological Society of India*, 74(1), pp. 78–94. Doi.org/10.1007/s12594-009-0093-x

[61] Yuguchi, T., Tsuruta, T., Nishiyama, T. (2011): Three-dimensional cooling pattern of a granitic pluton II: The study of deuteric sub-solidus reactions in the Toki granite, Central Japan. *Journal of Mineralogical and Petrological Sciences*, 106(3), pp. 130–141. Doi.org/10.2465/jmps.100129b

Original scientific article • DOI 10.2478/rmzmag-2021-0007

Received: June 11, 2021
Accepted: June 30, 2021

Valuation of Rubber Waste and Dune Sand: mortar for construction and environmental protection

Assia Aidoud[1,*] , Messaouda Bencheick[1], Salima Boukour[2]

[1]University 8 may 1945 of Guelma & Civil Engineering and Hydraulics Laboratory, Guelma, Algeria

[2]Civil Engineering and Hydraulic Laboratory, University Center of Abdelhafid Boussouf Mila, Mila, Algeria

*Corresponding author: E-mail: assia_aidoud76@yahoo.fr

Abstract

The main objective of this study is the recovery of dune sands and rubber waste (powders). The latter constitutes a potential source of several environmental and economic problems.

The objective of this present work is to examine the ability to use dune sand for the preparation of mortars with sufficient physico-mechanical properties to allow them to be used in various building construction applications. The formulation of the mixtures is based on replacing dune sand with powders, at different weight contents: 10 %, 20 %, and 30 %. The quantity of cement is set at 450 *g*. The results obtained show in the first place that the particle size of the mixture tends to be spread out with a remarkable increase in the fineness modulus, and in the second place the density of the mixture decreases by 6.5 % (for the apparent) and by 10 % (for the absolute), which means the calculation of loads for the resulting mortar must decrease. Porosity has decreased to 20 % and absorption has increased to 30%. The strengths have decreased over 40 % for compressive strength and over 30 % for tensile strength, with an improvement in the relationship between the two strengths.

Key words: Mortar, dune sand, rubber, porosity, absorption, strength

Introduction

In Algeria, the quality control bodies for structural concrete require that the aggregates are made from alluvial or quarry sands and crushed gravel. However, some projects, especially those carried out in the south, are far from the deposits exploited for the crushing of aggregates (more than 600 *km*). The energy expended for crushing and the budget reserved for the transport of crushed aggregates considerably amplifies the cost of producing one m^3 of concrete [1].

Southern Algeria has significant renewable natural reserves of dune sand, characterized by a fine grain size but with a chemical and mineralogical composition rich in silicon [2]. This paradox has prompted several scientists to search for a formulation devoid of coarse aggregate and therefore composed essentially of cement, filler, micro filler, sand and water [3–7].

Several studies have been carried out on mortars in order to know their formulations and to determine their characteristics and their rheological behavior. These studies have been able to prove that dune sand–based mortar could advantageously replace ordinary mortar in certain sectors of building and public works [8].

Waste from different sources is the cause of various environmental problems related to its storage and its increasing quantities. In addition, traditional building materials of natural origin are faced with exhaustion over time. It is therefore important to think about the development of composite materials with artificial aggregates, or those that are recycled from industrial and agricultural waste. This type of material meets economic and environmental requirements [9]. Indeed, the operation of industrial vehicles of different categories generates significant quantities of

tire waste, which does not benefit from any recovery action [10–11]. In Algeria, strong pressure on the environment has been recorded, especially with regard to waste from means of transport, specifically tires [12]. All over the world, used tire waste represents a potential source of major environmental and economic problems [10]. According to recent statistics, the annual world production of waste tires is estimated at 17 million tonnes. The latest global initiatives to reduce air pollution require the use of clean methods of waste disposal in order to protect the environment from its harmful effects [10].

The construction sector has been using waste and by-products for several years as secondary raw material for the development of new types of materials that have specific or improved properties compared to conventional materials. This alternative makes it possible on the one hand to respond to the concern for saving natural resources in aggregates, and on the other hand to alleviate economic and environmental constraints through the reuse and recycling of waste [13].

The objective of this work is the recovery of sand from dunes (DS) and the use of waste powdered tires in order to exploit them for the manufacture of mortar suitable for use in the construction sector. In our study we try to develop and characterize a rubberized sand mortar. This development is made by the addition of rubber content (RC). The formulation of the mixtures adopted is based on the mass substitution of dune sand by different percentages of rubber (10 %, 20 %, and 30 %). The quantity of cement is fixed at 450 *g* (based on the composition of a normalized mortar).

Experimental details

The materials used in this work for the preparation of the mixtures and the making of the various mortars are of local origin (Figure 1); their chemical compositions and their physical properties are shown in Table 1 and Table 2 respectively.

A control sand mortar, and three mortars composed of cement and by different percentages of (RC) (10 %, 20 % and 30 %) and dune sand, respectively (Figure 2 shows the mixes at different substitutions and Figure 3 shows the result for each mix) for each composition (Table 3) made the object of this comparative study. The tests concerned the determination

Figure 1: *The materials used, a) Dune sand, b) Cement, c) Rubber powder.*

Table 1: *Chemical compositions of cement and dune sand*

	CaO	SiO_2	Al_2O_3	Fe_2O_3	MgO	K_2O	Na_2O	SO_3	LoI*
Cement	58.6	24.92	6.58	3.65	1.21	0.85	0.08	2.17	1.7
Dune Sand	1.63	90.46	1.38	1.92	0.39	0.22	0.00	0.2	2.56

* Loss on Ignition

Table 2: *General material properties*

	Unit	Dune Sand	Cement	RC
Finess modulus	(%)	1.837	-	3.92
Sand equivalent (visual)	(%)	99.56	-	-
Sand equivalent (piston)	(%)	85.97	-	-
Apparent density	(g/cm^3)	1.46	1.09	0.40
Absolute density	(g/cm^3)	2.11	3.11	0.94
BSS	(cm^2/g)	-	3371	-

*Blain Specific Surface

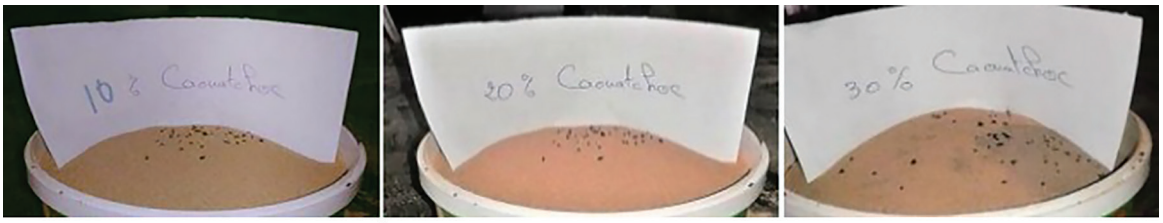

Figure 2: *The three mixtures of DS with the three substitutions: a) 10%, b) 20% and c) 30%.*

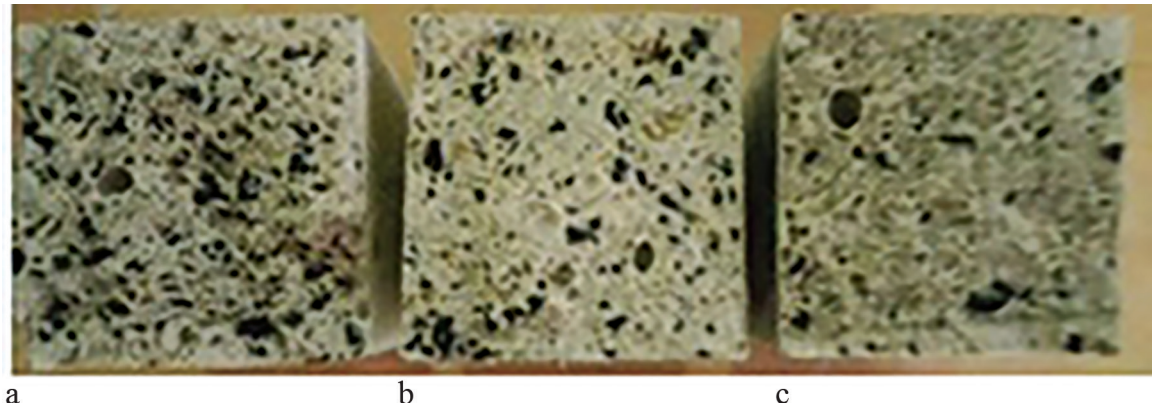

Figure 3: *The three mortars made with DS mixes with three substitutions: a) 30%, b) 20% and c) 10%.*

of some physico-mechanical properties of the mortars (porosity, absorption, densities, compressive strength, tensile strength). All the tests were carried out on prismatic specimens (4 *cm* x 4 *cm* x 16 *cm*).

The compression (Figure 4) and tensile tests (by three-point bending) (Figure 5) were carried out by a universal digital CONTROLS brand mechanical resistance testing machine with a capacity of 50 *kN*, at controlled load and displacement. The measurements of the physical properties were carried out by a hydrostatic balance precision of 0.01 *g*.

Effect of rubber on the physico-mechanical properties of the mortar

The various results are grouped together in the table and illustrated by the figures below.

Table 3. *Composition of the mortars studied*

Rubber content (%)	0	10	20	30
Dune Sand (g)	1350	1215	1080	945
Cement (g)	450	450	450	450
Water (g)	450	450	450	450
Rubber Caoutchouc (g)	0	60.14	120.28	180.42
Water/Cement	1	1	1	1

Figure 4: *The compression test.*

Figure 5: *The three-point flexural tensile test.*

Effect of rubber on the physical properties of the mortar

With each increase in the content of substituted rubber in the sand, the grain size curve of the mixture tends to spread out (Figure 6).

The fineness modulus of the mixtures increases with the increase in the content of rubber (Figure 7).

For a mixture of DS substituted with 10 % rubber, the fineness modulus increased by 5 % compared to the fineness modulus of the control DS, but despite the substitution of the DS at 20 %, a slight increase of 7 % was noticed of the fineness modulus relative to the fineness modulus of the control DS. On the other hand the increase was very remarkable (20 %) for the mixture of DS substituted for 30 % of the rubber.

It can also be seen that despite these increases in fineness moduli, our mixtures still remain within the fine sands interval. But what caught our attention that the finesse modulus jumped between the two ends of this interval.

All DS-based mortars with RC substitutions of 10 %, 20 %, and 30 % experience decreases in their densities either wet or dry (Figure 8) compared to the control mortar, of the order of 2.86 %, 5.71 %, and 6.86 % and 0.64 %, 3.85 %, and 5.13 % respectively. This is particularly useful in rehabilitation works and the lightening of structures. These decreases are less important than those found by Benazzouk et al. [13] and by Boukour [14].

According to Figure 8, the wet density of the mortar varies according to the rubber

Table 4: *Effect of rubber on the physico-mechanical properties of the mortars studied*

Rubber content (%)	0	10	20	30
Fineness modulus (%)	1.837±0,027	1.93±0,043	1.98±0,056	2.20±0,068
Wet density (g/cm^3)	1.75±0.026	1.7±0.016	1.65±0.004	1.63±0.013
Dry density (g/cm^3)	1.56±0.045	1.55±0.023	1.5±0.006	1.48±0.01
Absorption (%)	12.1±1.85	9.81±0.62	9.77±0.08	10.64±0.12
Porosity (%)	18.86±2.39	15.21±0.73	14.69±0.09	15.71±0.27
Tensile strength (MPa)	5,47±1.11	4.95±0.31	4,71±1.41	3,36±0.61
Compressive strength (MPa)	26,51±2.46	18,44±0.29	17,33±0.77	14,01±1.00

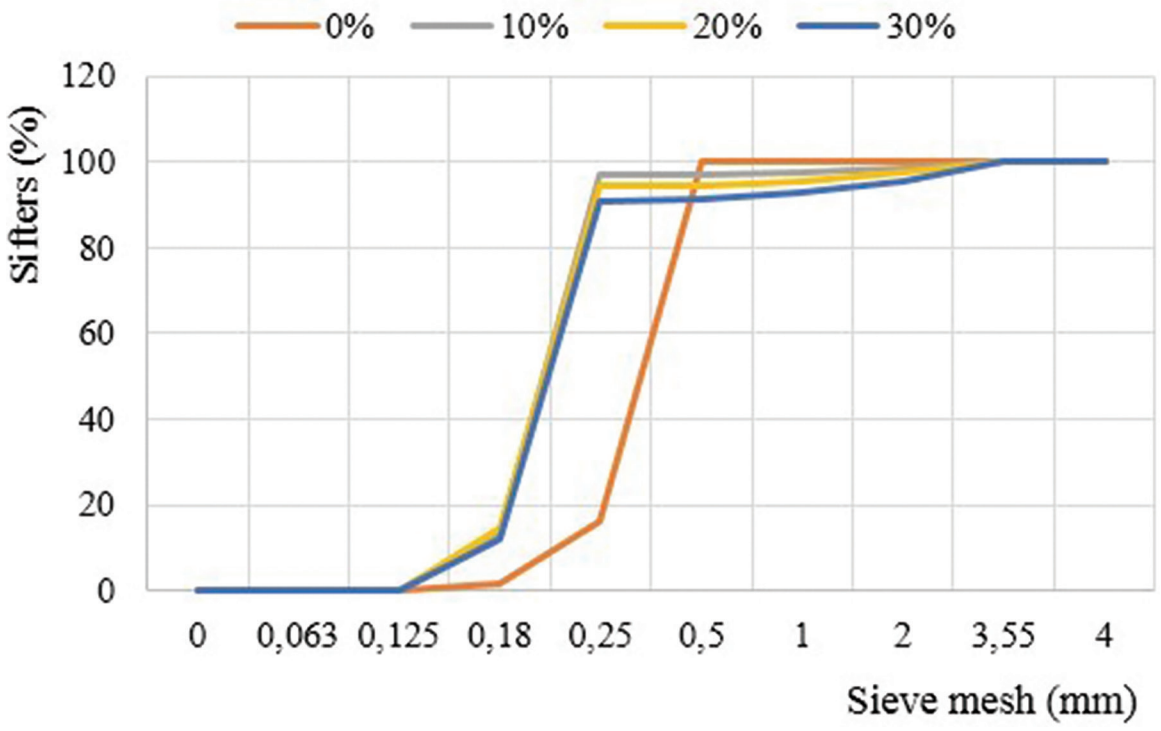

Figure 6: *Particle size curves of the mixtures as a function of the rubber content.*

content, according to the expression: Wd = 0.0075 (% RC)^2 - 0.0785 (% RC) + 1.8225 with a correlation coefficient: R^2 = 0.9948. And the dry density of the mortar varies according to the rubber content according to the expression: Dd = -0.0025 (% RC)^2 - 0.0165 (% RC) + 1.5825 with a correlation coefficient: R^2 = 0.9453.

It is worth noting that reductions in water absorption during total immersion are approximately 18.92 % to 19.25 % for mortar based on dune sand and with the substitution of rubber content of 10 % and 20 % respectively, as shown in (Figure 9). These results are in accordance with the findings of various authors for the incorporation of rubber aggregates in cement matrix and with zero absorption of rubbers [15–16] cited by Boukour [14]. This is surely due to a probable decrease in the porosity of these mortars. On the other hand, there was a return in the decrease in absorption of the order of 7.18 % for the DS-based mortar and with 30 % of RC substitutions, different from the result found by Boukour [14]

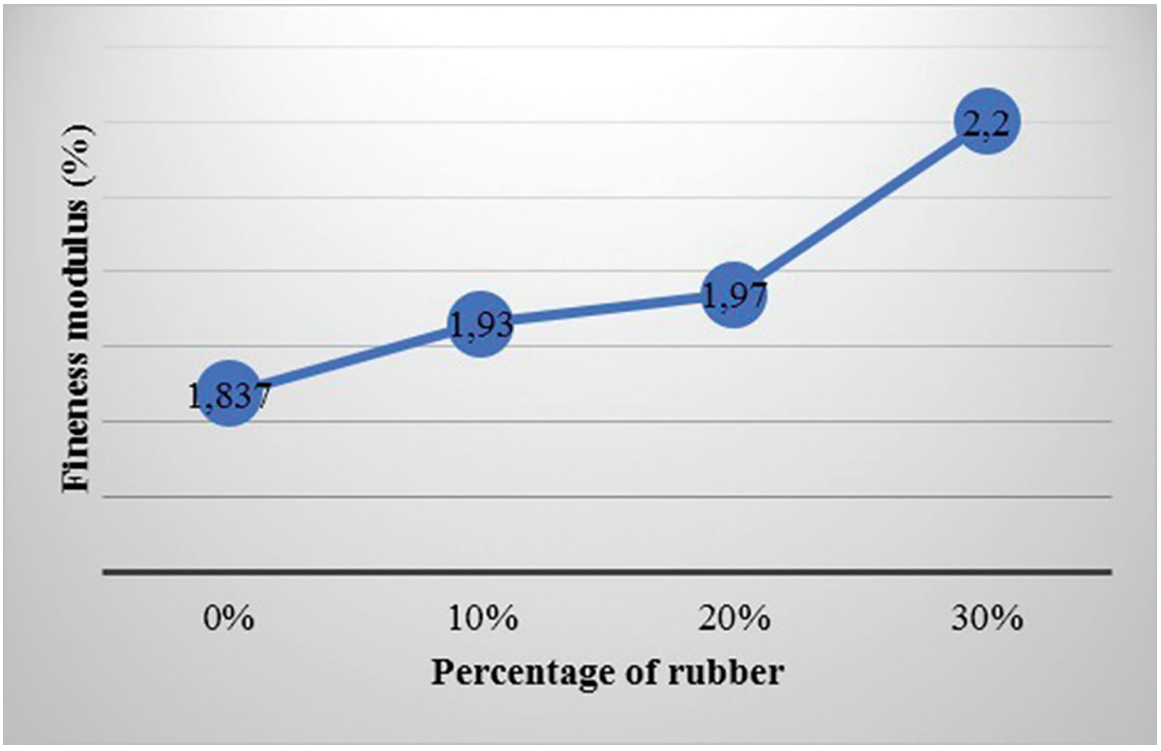

Figure 7: *Evolution of fineness modulus as a function of rubber content.*

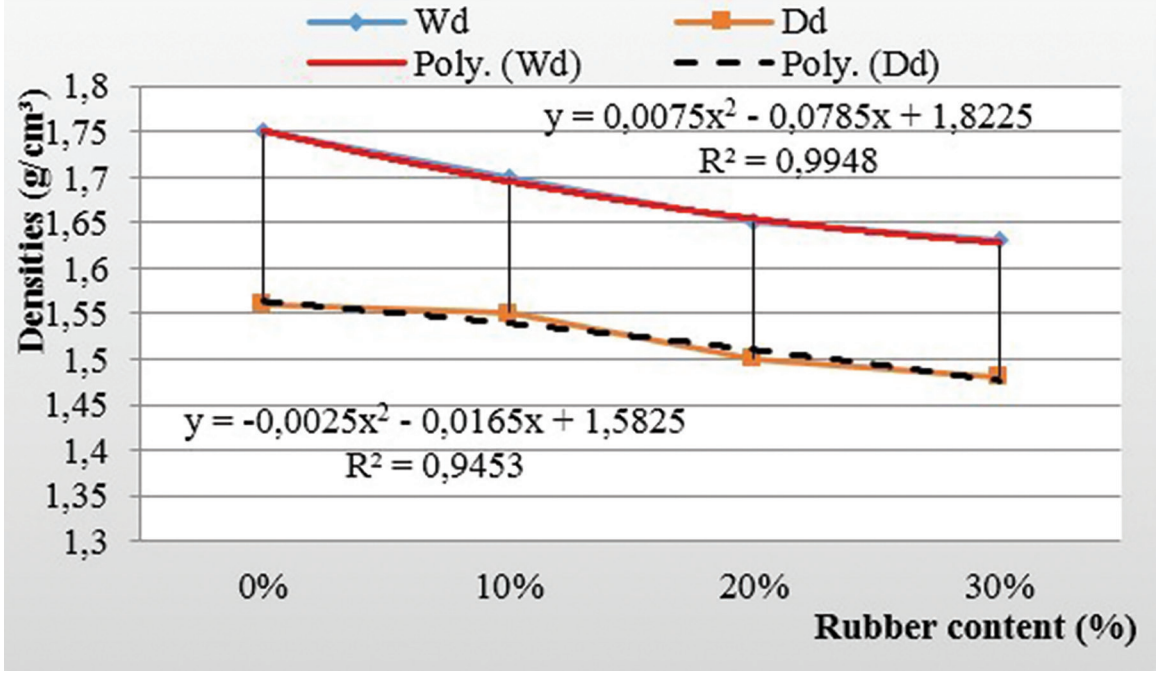

Figure 8: *Evolution of density as a function of rubber content.*

for this percentage of substitution. Our result could be related to the pores generated by this amount of RCs due to their non-polar natures and their smaller size compared to RAs (rubber aggregates), which tend to trap surface air. The air trapped in this mortar makes the mortar more porous, therefore more permeable and more water-absorbent.

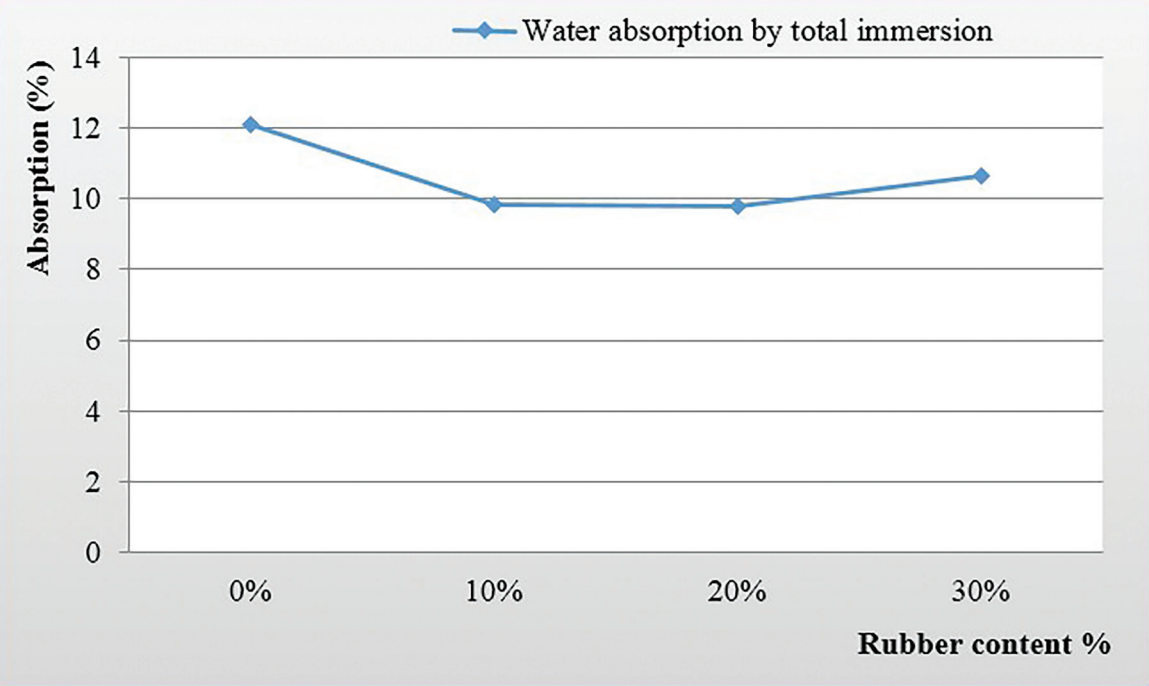

Figure 9: *Evolution of absorption by total immersion depending on the rubber content*

The decrease in porosity (Figure 10) reached 19.35 % and 22.11 % respectively for sand mortars with 10 % and 20 % substitutions of DS by RC, which confirms the findings noted above concerning the possibility of a decrease in DS porosity, especially at 10% of substitutions of DS by RC. This is contrary to the results of other authors, which indicate that the occluded air entrained by the RA during mixing is a factor favouring the increase in porosity [17–19]. At 30 % substitutions of DS by RC, the return is also noticed (5.42 %). Note that other authors [20–21] suggest that the hydrophobic nature of RA is responsible for trapping air bubbles, which contributes to the lightening of RA composites.

Effect of rubber on the mechanical properties of the mortar

It can be seen from Figure 11 that the substitution of dune sand by rubber content reduces resistance, while the tensile strength decreases slightly, usually on the order of 9.51 % to 13.89 % with substitution of 10 % and 20 % respectively; reduction in tensile strength is very significant at 30 % substitution (38.57 %). On the other hand, for compressive strength the decreases are more than 30 % for the three substitutions (10 %, 20 %, and 30 %) on the order of 30.44 %, 34.63 %, and 47.15 %, respectively. This loss of mechanical performance, according to Guelmine et al. [10] is mainly linked to the poor adhesion of the rubber particles to the cement matrix. Most remarkable are the decreases in both mechanical resistances at 30 % substitution, which can lead us to limit the percentage of substitution to less than 30 %. But despite that, this loss remains less than that found by Boukour [14].

Effect of rubber on the relationship between the mechanical properties of the mortar

The relationships between strengths (compressive and tensile) can be influenced by the substitution of DS by RC. It has been observed through the results of these properties that they can present different values. In this part of the work, we explore the effect of rubber on these relationships, between compressive strengths and tensile strengths (Figure 12). These relations between properties are also situated in relation to those given by the regulations Eurocode EC2 [22] and the Unified Document DTU [23].

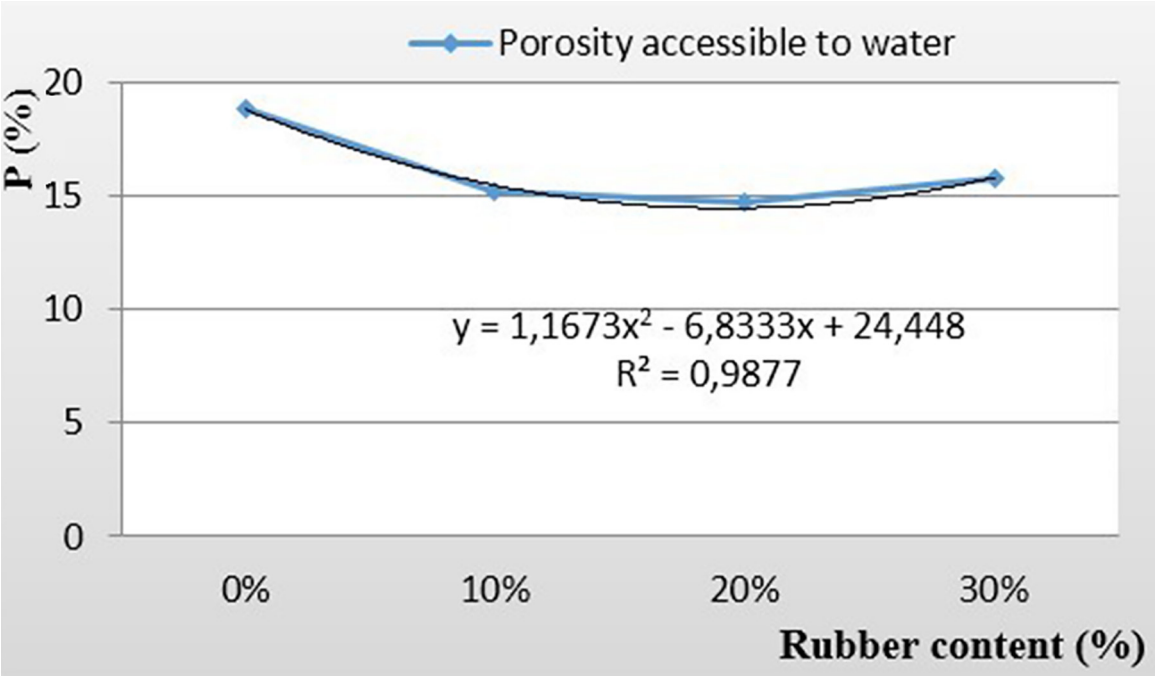

Figure 10: *Evolution of porosity accessible to water as a function of rubber content.*

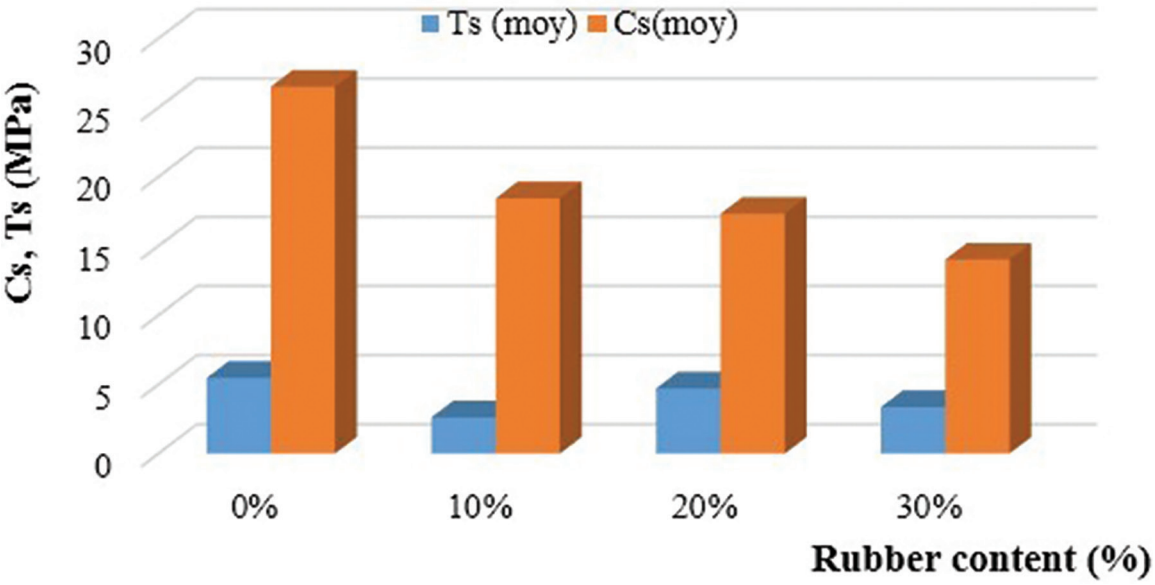

Figure 11: *Evolution of the compressive and tensile strength as a function of the rubber content.*

Relations between compressive strengths and tensile strengths

The preceding curves (Figure 12) show the Ts-Cs (Tensile strength and Compressive strength) relationships for rubberized sand mortars at 0 %, 10 %, 20 %, 30 % of RC. We notice that the difference between the regulatory curves and the experimental curve of the mortars studied is also important despite the reverse direction of the evolution (decrease depending on the rubber content) with a very acceptable regression quality Rt-Rc (R^2 = 0.9988).

The Ts-Cs relation of rubberized sand mortars at 0 %, 10 %, 20 %, 30 % of RC always gives

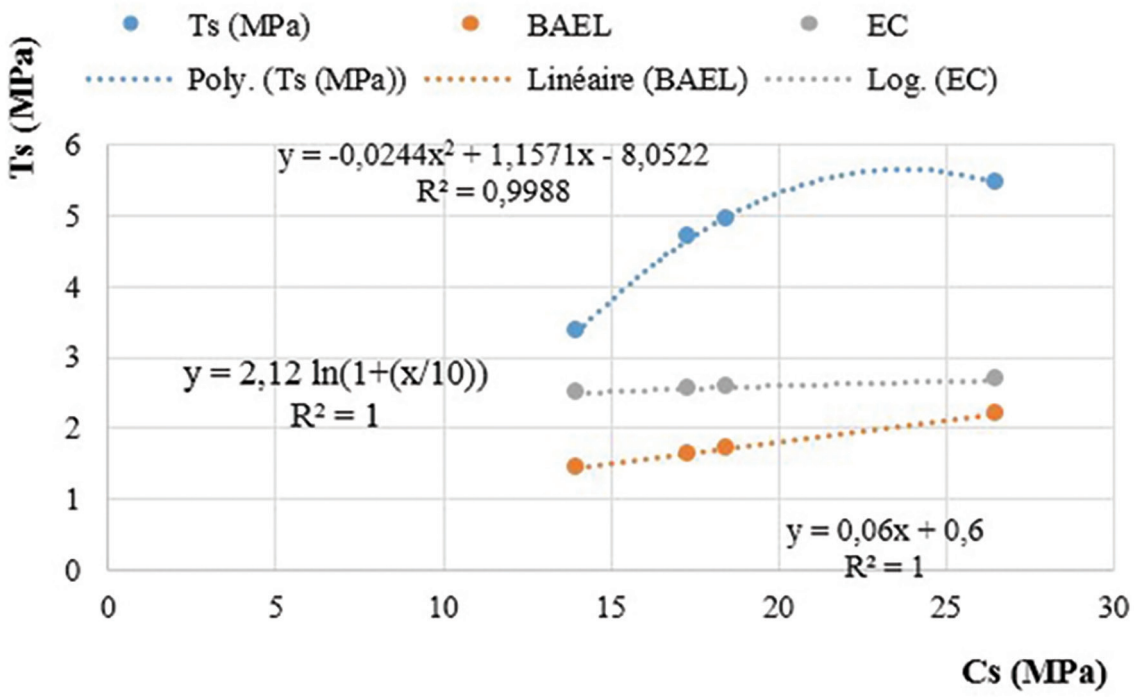

Figure 12: *Relations between compressive strengths and tensile strengths.*

overestimated values, but of course not at the same pace as those of the regulations (polygonal relation) these values are influenced by the presence of dune sand in the compositions of the mortars.

It can be seen that the Ts-Cs relationships are influenced by the percentage of dune sand substitution by RC.

Conclusions

The correction of the grain size of the DS is possible by the RC. This is clearly verified by the fineness modulus, which marked a jump between the two ends of the fine aggregate interval. This improvement is noticed especially at 30 % substitution.

Rehabilitation work and the lightening of structures are based mainly on the values of the densities of the construction materials. The decrease in the values of the latter is noticed for the three substitutions (10 %, 20 %, and 30 %) but is less important than those found by several other authors. They follow polygonal functions of order 2 with correlation coefficients very close to 1.

A positive effect for absorption by total immersion is found up to 20 % substitution of DS by RC. On the other hand, at 30 % of substitutions the absorption increased.

The effect of the substitution of DS by RC on the porosity of the mortars is the same as that of the absorption, with different values (decrease in up to 20 % of substitution and an increase in up to 30 % of substitution).

The percentage of substitution of DS by RC can be limited to less than 30% because of its detrimental effect on the two mechanical resistances.

The relation which connects the two mechanical resistances (traction and compression) is influenced by the percentage of substitution of dune sand by RC. It presents estimates greater than those of the normative documents, by following a polygonal function of the order 2 with a correlation coefficient very close to 1.

Acknowledgements

The authors thank the LGCH research laboratory at the University 8 May 1945 (Guelma) and the pedagogical laboratory of the civil and hydraulic engineering department (Guelma) for their technical support during the experimental work.

References

[1] Bouaziz, A., Hamzaoui, R., Rezigue, S., Bennabi, A. (2013): Valorization of dune sand in formulations of mortars and concrete. In: *31st AUGC Meetings, E.N.S*. Cachan, May 29 to 31, pp.1-11.

[2] Boudaouad, Z., Breysse, D. (2002): Study of the effects of co-grinding of a sand and a clinker on the properties of concrete. *Materials and Structures,* 5 (35), pp. 310-316, DOI: https://dx.doi.org/10.1617/13734.

[3] Bilhout, H., Dilude, P. (1994): *Sand concrete.* Paris, Jouve, p. 11.

[4] Cisse, K., Lauuerbe, M., Gaye, A., Diene, M. (1999): Characterization of compacted road sand concretes: application to the case of Senegal. *Materials and Construction,* 32 (216), pp. 151-157.

[5] Cissé, K., Lauuerbe, M. (2000): Mechanical characterization of filler sand concrete with rice husk ashes addition: study applied to Senegal. *Cement and Concrete Research*, 30 (1), pp. 13-18, DOI: https://doi.org/10.1016/S0008-8846(99)00182-9

[6] Benaiss, A., Morlier, P., Tram, V. (1992): Concrete sand, a non-cracking material. *Francis Jeanson National School of Public Works , Algeria equipment*, *(materials)* pp. 7-10.

[7] Tafraoui, A. (2009): *Contribution to the recovery of sand from the western erg dunes (Algeria). Application to new concretes*, PhD thesis, University of Toulouse, 223 p.

[8] Belkhiri, H., Derragui, A. (2016): *Contribution to the study of the mechanical behavior of dune sand and fine siliceous mortar*. Master's thesis, Geotechnics & Materials: Ziane Achour University of Djelfa, 74 p.

[9] Menadi, S., Benazzouk, A., Douzane, O., Merzoud Mohamed, M., Habita, F., Langlet, T. (2013): Study of the feasibility of a composite with a cement matrix reinforced with jute fibers. Synthesis: *Revue Science Technology syntheses*, (27), pp. 40-49.

[10] Guelmine, L., Hadjab, H., Benazzouk, A. (2018): Effect of recycled rubber granulates on used tires on the physical and mechanical properties of cement mortar. In: *International Civil Engineering Seminar, "IACS"*.

[11] Ho Anh Cuong, M. (2010): *Optimization of the composition and characterization of a concrete incorporating aggregates from the grinding of used tires: Application to large surface elements*. PhD thesis, University of Toulouse, 250 p.

[12] Hamlaoui, C.A., Moussaoui, H. (2019): *Valorization of rubber waste from tires and glass waste in sand concrete*. Master's thesis: Materials in Civil Engineering, University Akli Mohand Oulhadjde Bouira. 139 p.

[13] Benazzouk, A., Douzane, O., Quéneudec, M. (2006): Recovery of rubber waste in construction materials: case of a cellular cementitious composite. *dechets-sciences-techniques*, 41 (1), pp. 30-35, DOI: 10.4267/dechets-sciences-techniques.1762

[14] Boukour, S. (2017): *Physico-mechanical characteristics and durability of cement eco-composites based on rubber aggregates from used tires*, PhD thesis, University of 8 May, 1945 Guelma, 237 p.

[15] Nehdi, M., Khan, A. (2001): Cementitious composites containing recycled tire rubber: an overview of engineering properties and potential applications. *Cement, Concrete and Aggregates*, 23(1), pp. 3-10, DOI: https://doi.org/10.1520/CCA10519J

[16] Price, W., Smith, E.D. (2006): Waste tire recycling: environmental benefits and commercial challenges. *International Journal of Environmental Technology and Management*, 6(3/4), pp. 362-374.

[17] Benazzouk, A., Douzane, O., Langlet, T., Mezzeb, K., Roucoult, J.M., Quéneudec, M. (2007): Physico-mechanical properties and water absorption of cement composite containing shredded rubber wastes. *Cement Concrete Composite*, 29 (10), pp. 732-740, DOI: https://doi.org/10.1016/j.cemconcomp.2007.07.001.

[18] Fadiel, A., Al Rifaie, F., Abu-Lebdeh, T., Fini, E. (2014): Use of crumb rubber to improve thermal efficiency of cement-based materials. *American Journal of Engineering and Applied Sciences*, 7 (1), pp. 1-11, DOI: https://doi.org/10.3844/ajeassp.2014.1.11.

[19] Eiras, J.N., Segovia, F., Borrachero, M.V., Monzó, J., Bonilla, M., Payá, J. (2014): Physical and mechanical properties of foamed Portland cement composite containing crumb rubber from worn tires. *Materials and Design*, 59, pp. 550-557, DOI: http://dx.doi.org/10.1016/j.matdes.2014.03.021.

[20] Hernandez-Olivares, F., Barluenga, G. (2004): Fire performance of recycled rubber-filled high-strength concrete. *Cement and Concrete Research*, 34(1), pp. 109-117, DOI: https://doi.org/10.1016/S0008-8846(03)00253-9.

[21] Siddique, R., Naik, T.R. (2004): Properties of concrete containing scrap-tire rubber–an overview. *Waste*

Management, 24(6), pp. 563-569. DOI: https://doi.org/10.1016/j.wasman.2004.01.006.

[22] EUROCODE 2 (ENV 1992-1-2): *Design of concrete structures, Part 1-2*: General rules - calculation of fire behavior. February 2001.

[23] BAEL 91 rules (DTU P 18-702) (revised February 99, 2000) *Technical rules for the design and calculation of reinforced concrete structures and structures using the limit states method Fascicle 62, title 1 of the CCTG - Works section 1*: reinforced concrete 1.

Original Scientific Article • DOI: 10.2478/rmzmag-2021-0014

Received: April 17, 2021
Accepted: April 21, 2021

Analysing the rate of land use and land-cover changes in Gambari Forest Reserve, Nigeria

Analiziranje sprememb rabe in pokrovnosti tal na območju gozdnega rezervata Gambari v Nigeriji

J. O. Mephors[1,*], O. D. Onafeso[2], O. S. Afolabi[1], O. J. Aigbokhan[1], I. S. Adamu[3]

[1]Department of Environmental Modelling and Biometrics, Remote Sensing and GIS Section, Forestry Research Institute of Nigeria, Ibadan, Nigeria

[2]Department of Geography, Olabisi Onabanjo University, Ago-Iwoye, Nigeria

[3]Department of Environmental Modelling and Biometrics, Climate Change Section, Forestry Research Institute of Nigeria, Jericho, Ibadan, Oyo State, Nigeria

*Corresponding author: E-mail: : justinaalagbe@gmail.com

Abstract in English

This research work discusses the phenomenon of land use and land cover, which has undergone constant changes over the past few decades due to major variations in the environment caused by anthropogenic and natural factors. This study is supported by a long time series of land use and land-cover satellite data of the Gambari Forest Reserve boundary map for 1984, 2004, and 2020. A maximum likelihood classification scheme was employed to classify the satellite imageries using ArcGIS 10.1 software to derive the spatial patterns and temporal variation of the land-use and land-cover change (LULC) classes: dense forest (DF), light forest (LF) and non-forest (NF). Data on deforestation of the study area showed that the area of DF increased from 31.7 km^2 (23.4%) to 72.8 km^2 (54.4%) within a 36-year time series, with a percentage change of 31.0%. The area of LF decreased from 79.2 km^2 (65.4%) to 51.2 km^2 (41.5%), with a percentage change of −23.9%, and that of NF decreased from 14.7 km^2 (11.2%) to 2.6 km^2 (4.1%), with a percentage change of −7.1%. This indicates that it would be reasonable to anticipate an increase in deforestation in the future.

Keywords: geospatial technique, LULC, change detection, deforestation, mapping

Abstract in Povzetek

Raziskava se osredotoča na pojave rabe in pokrovnosti tal, ki se je v zadnjih nekaj desetletjih stalno spreminjala zaradi večjih okoljskih sprememb, povzročenih z antropogenimi in naravnimi dejavniki. Raziskava je osnovana na dolgoletnih satelitskih podatkih iz leta 1984, 2004 in 2020 o rabi in pokrovnosti tal na območju gozdnega rezervata Gambari. Za razdelitev satelitskih posnetkov v razrede rabe in pokrovnosti tal – LULC (gosti gozd, redek gozd, negozd) je bila uporabljena klasifikacija maksimalne verjetnosti s pomočjo programske opreme ArcGIS 10.1. Rezultati posnetkov na raziskovanem območju v obdobju 36 let so pokazali, da se je gosti gozd povečal iz 31.7 km^2 (23.4%) na 72.8 km^2 (54.4%) s spremembo 31.0%. Redki gozd se je zmanjšal iz 79.2 km^2 (65.4%) na 51.2 km^2 (41.5%) s spremembo −23.9%. Negozd se je zmanjšal iz 14.7 km^2 (11.2%) na 2.6 km^2 (4.1%) s spremembo −7.1%. To dokazuje da je verjetnost za krčenje gozdov v prihodnosti visoka.

Ključne besede: geoprostorske tehnike, LULC, zaznavanje sprememb, krčenje gozdov, kartiranje

Introduction

As an important part of worldwide sustainable development, land -use and land-cover change (LULC) and deforestation in Nigeria have attracted great attention. LULC has been considered as an important research topic for global environmental change and sustainable development [1]. Land cover refers to the biophysical attributes of the Earth's surface, while land use refers to the human purpose or intent applied to these attributes [1]. Deforestation is an important process of LULC [2], and it is also a factor that provides feedback for the drivers of land-use change [3]. However, examining the process and trends of LULC via quantitative analysis is a prerequisite for gaining a deeper understanding of LULC and help policy makers set improvement targets in specific areas and adopt appropriate practices while also keeping in line with other fields of sustainability [2,4, 5,6]. The acceleration of urbanisation and industrialisation has led to serious ecological destruction, such as a decrease in ecological carrying capacity, vast coverage and intensity of water and soil loss, desertification, soil erosion, vegetation degradation, biodiversity losses, invasion of alien species, environmental pollution, natural hazards, geological hazards, and forest hazards [7].

LULC is the conversion of different land-use types and is the result of complex interactions between humans and the physical environment [8]. Therefore, accurate and up-to-date land-cover change information is necessary for understanding and assessing LULC changes. Remote sensing (RS) and geographic information systems (GIS) are essential tools that are used to obtain accurate and timely spatial data of land use and land cover, as well as to analyse the changes in a study area [9,10]. RS images can effectively record land-use situations and provide an excellent source of data from which updated LULC information and changes can be extracted, analysed, and simulated efficiently through certain means [11,12]. Therefore, RS is widely used in the detection and monitoring of land use at different scales [13–15]. GIS provides a flexible environment for collecting, storing, displaying, and analysing digital data necessary for change detection [9,16,17]. The present study aims to assess the changes that occurred in Gambari Forest Reserve, Nigeria, within the period of the 32 years from 1984 to 2016. The objective of this study is to examine the LULC changes in the study area between 1984 and 2016.

Study Area

Gambari Forest Reserve is located between latitude 7°10′51″N and longitude 3°52′34″E. Figure 1 shows the natural forest reserve plot at 6.5 km from the Cocoa Research Institute of Nigeria (CRIN), on the Idi-Ayunre-Ijebu-Ode Road, Oyo State.

Gambari Forest Reserve has one of the most complex vegetation types with the highest number of plant species per unit area. This vegetation is dominated by woody trees to the exclusion of grasses; grasses are shade-intolerant and cease to grow under such tall vegetation, which has a heavy total canopy [19]. The topography of the study area is generally undulating with the presence of lianas, climbers, twiners, stranglers, scramblers, and epiphytes, which makes movement almost impossible. The valuable indigenous species are *Terminalia spp* K. Shum (Afara), *Triplochiton scleroxylon* K. Shum (Arere, Obeche), *Irvingia garbonensis* (Oro) and *Treculia africana*, among others. Exotic species such as *Gmelina arborea* (Gmelina) and *Tectona grandis* (teak) are found in the study area. The study area lies at an altitude between 90 m and 147 m above sea level [20]. The study area is bounded by two rivers (rivers Ona and Awon).

The major dry season occurs between December and March. Temperatures are high throughout the year, with a mean annual value of about 27°C and an annual range of 30°C [18,21].

Materials and Methods

In this study, the sources of data collected are the Landsat satellite RS images for 1984, 2004, and 2020 with a resolution of 30 m. This study will also show how the data are collected and the methods of analysis used.

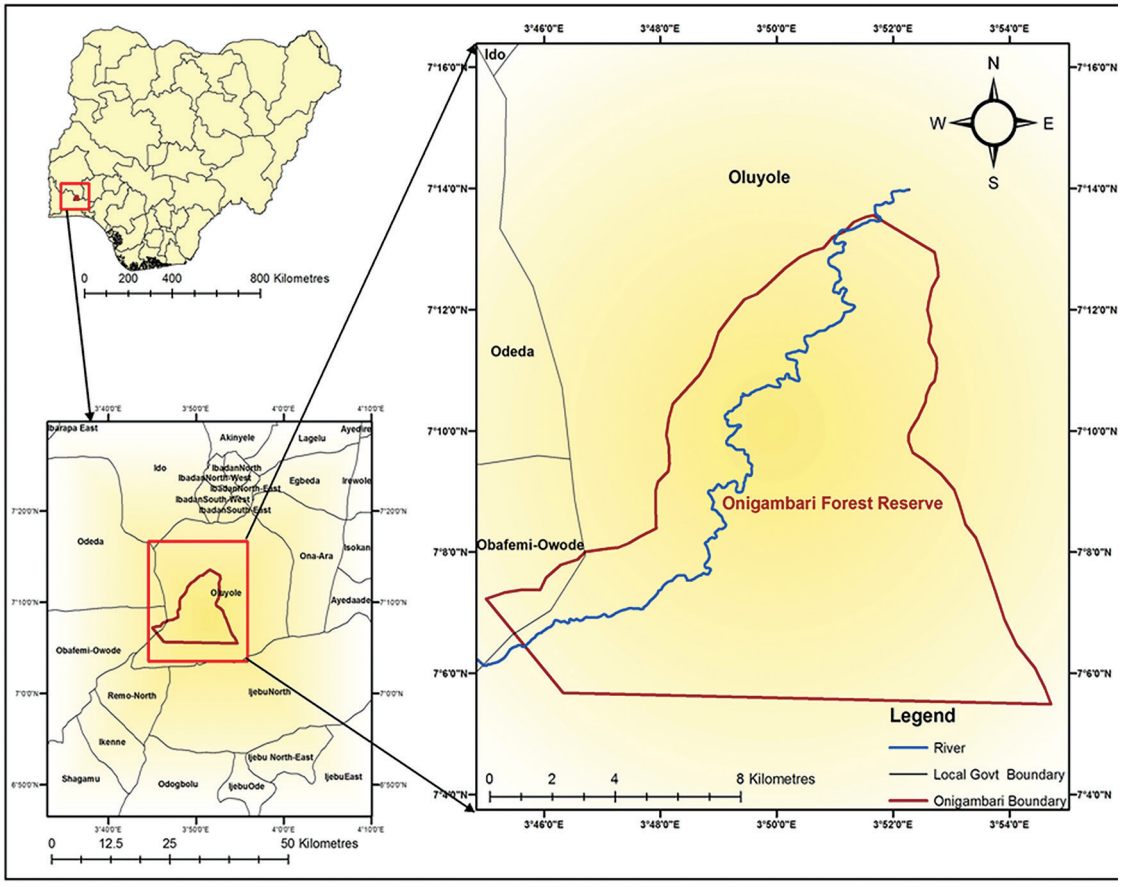

Figure 1: *Map of the study area (Gambari Forest Reserve).*
Source: Adapted from the study by Adedeji et al. [18].

Table 1: *Data set acquired and its sources*

S/N	Data Sets	Resolution/ Scale	Year of Production	Date of Acquisition	Source
1	Landsat 5	30 M	1984	18/12/1984	USGS
2	Landsat 7	30 M	2004	06/02/2004	USGS
3	Landsat 8 OLI	30 M	2020	15/02/2020	USGS
4	Gambari Forest Reserve boundary map	1:50,000	2015	23/11/2018	Adedeji et al. [18]

Collection of Satellite Data

Landsat images of the study area for three different years with the space span intervals of 20 and 16 years (for 1984, Landsat 5; for 2004, Landsat 7; and for 2020, Landsat 8 OLI) are used for this study, and the orthorectified images for 1984, 2004, and 2020 were downloaded from the United States Geological Survey (USGS), as shown below (Table 1). The software package ArcGIS 10.1 (2013) version was used to visually and digitally process and interpret the Landsat satellite images.

RS Image Pre-processing and Accuracy Verification

The RS image data of 1984, 2004, and 2020 were radially calibrated and atmospherically corrected. The relative geometric corrections of the three images were conducted to remove geometric distortion caused by the sensor or

Table 2: *LULC classification scheme*

S/N	Code	LULC Classification Category	Definition of Terms
1	DF	Dense forest	Area with dense intensity of forest with thick closed canopy
2	LF	Light forest	Area with low intensity of forest with light closed canopy
3	NF	Non-forest	Area covered with shrubs and grasses with no canopy

GPS is used for navigation, location of sample plots and recording of coordinate points. Ground distance is measured by surveyors using a tape.

the Earth's rotation. Considering the study area and the goal of this study, the land-use types are divided into three categories: dense forest (DF), light forest (LF) and non-forest (NF) (as shown in Table 2). With the help of the maximum likelihood method classifier, classification was carried out on these three images.

Results and Discussion

The data collected and analysed for this study are satellite images that are classified and presented in the form of maps and statistical tables and represent the analysis of the various research data used in this study.

Trend in the LULC distribution of the Gambari Forest Reserve in 1984

The Gambari Forest Reserve area in 1984 recorded more LF than NF. DF covered an area of 31.7 km^2 (23.4%), while LF covered 79.2 km^2 (65.4%), and NF covered 14.7 km^2 (11.2%), as shown below (Table 3). The LULC distribution for the study area in 1984, as derived from the map, showed that LF occupied the largest class, with 65.4% of the total classes, which implies that the forest reserve was still intact or minimally tampered with at the time under study. The Gambari Forest Reserve is a reserved area allocated to the Forestry Research Institute of Nigeria for experimental purposes, which restricted the Gambari Forest from being encroached (Figure 2).

Trend in the LULC Distribution of the Gambari Forest Reserve in 2004

The static LULC change detection for the Gambari Forest Reserve area in 2004, as derived from the imagery, indicates that there

Table 3: *LULC distribution of Gambari Forest in 1984 showing area (km^2) of the LULC classes*

Classes	Area (%)	Area (km^2)
Non-forest	11.20	14.70
Light forest	65.40	79.20
Dense forest	23.40	31.70
TOTAL	100.00	125.60

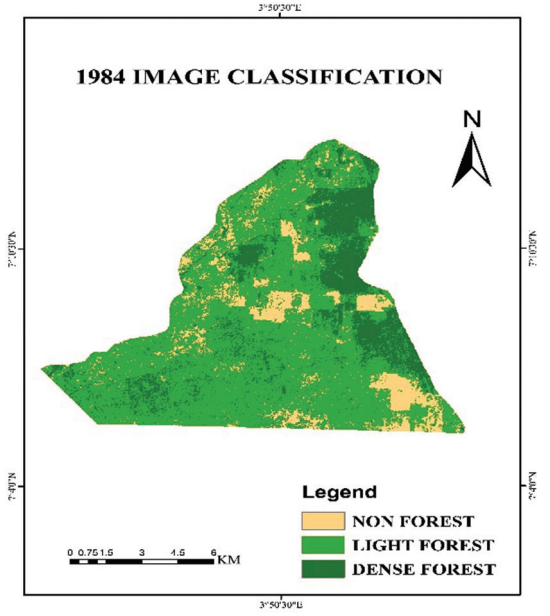

Figure 2: *Land-cover classification of Gambari Forest in 1984.*

is a significant increase in DF and NF areas, while the area of LF reduced over the 20 years (1984–2004). DF covered an area of 36.6 km^2 (31.2%), while LF covered 51.2 km^2 (43.7%), and NF covered 37.8 km^2 (25.1%), as shown in Table 4.

The area of DF increased from 23.4% in 1984 to 31.2% in 2004, which resulted from re-afforestation (amounts to 7.8%), while the area of LF decreased from 65.4% in 1984 to 43.7% in 2004, which implied a percentage size loss of –21.7% due to anthropogenic activities

Table 4: *LULC distribution of Gambari Forest in 2004 showing area (km²) of the LULC classes*

Classes	Area (%)	Area (km²)
Non-forest	25.10	37.80
Light forest	43.70	51.20
Dense forest	31.20	36.60
TOTAL	100.00	125.60

Table 5: *LULC distribution of Gambari Forest in 2020 showing area (km²) of the LULC classes*

Classes	Area (%)	Area (km²)
Non-forest	4.10	2.60
Dense forest	54.40	72.80
Light forest	41.50	51.20
TOTAL	100.00	125.60

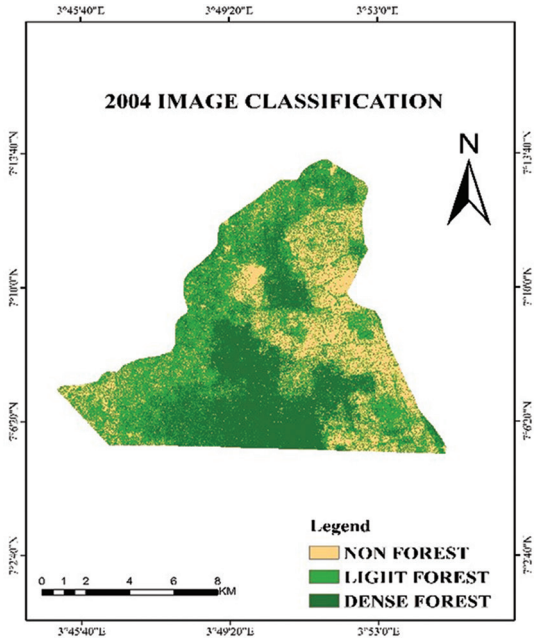

Figure 3: *Land-cover classification of Gambari Forest in 2004.*

such as selective logging and legal felling, which led to the reduction of the volume of trees left in the area.

For the NF area, there was also a geometric increase from 11.2% in 1984 to 25.1% in 2004, which implies that a percentage size of 13.9% could be a result of the above stated anthropogenic activities such as major felling of trees without replanting (Figure 3).

Trend in the LULC Distribution of the Gambari Forest Reserve in 2020

The Gambari Forest Reserve area in 2020 recorded more DF than LF. DF covered an area of 72.8 km² (54.4%), while LF covered 51.2 km² (41.5%), and NF covered 2.6 km² (4.1%).

An assessment of the classification data in 2020 imagery reveals that there has been a transition in the status of the forest reserve in the span of 36 years, which indicates that the DF area increased from 23.4% in 1984 to 54.4% in 2020, which implies a percentage change of 31.0%, due to favourable environmental factors such as climatic weather, decomposition, and conservation.

For the LF area, it was established that there was a decrease from 41.5% in 2020 to 65.4% in 1984, with a percentage variation of −23.9%, which is a decrease from what was classified in 1984. This could be as a result of poor management of the experimental plots, illegal fellers, and climate variability.

Furthermore, the NF status stands at 4.1% in 2020, which is also a decrease compared to 11.2% in 1984, with a percentage variation of −7.1% due to increase in sizes of both the DF and LF, respectively, which increased their LU over time.

The LULC distribution for the study area in 2020, as derived from the map, shows that DF occupied the largest class, with 54.4% of the total classes due to anthropogenic activities that occurred to the other classes (Table 5, Figure 4).

Changes in Land Cover of Gambari Forest Reserve from 1984 to 2004

The changes outlined in Table 6 occurred over the past 20 years in the Gambari Forest Reserve area from 1984 to 2004, where changes of the land covers are presented. LF declined in percentage size drastically by −21.7%, NF increased drastically by 13.9%, while DF also increased by 7.8%.

Changes in Land Cover of Gambari Forest Reserve from 2004 to 2020

The changes mentioned below occurred over the past 16 years in the study area during

2004–2020. As shown in Table 7, representing 2004 to 2020 satellite images, changes of the land cover during this period show that DF changed by 23.20%, LF changed by – 2.20%, and NF changed by – 21.00%.

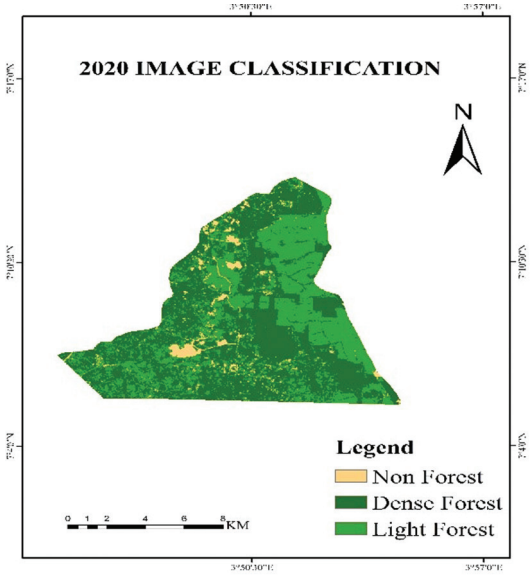

Figure 4: *Land-cover classification of Gambari Forest in 2020.*

Changes in Land Cover of Gambari Forest Reserve from 1984 to 2020

The overall trend of thr e36-year change that occurred between 1984 and 2020—as shown in Table 8—indicates that the DF area positively increased in percentage change by 31.00%, from 31.7 km² (23.4%) to 72.8 km² (54.4%), which could be as a result of environmental factors such as climatic weather, decomposition, and conservation. The LF area decreased in percentage change by –23.9% from 79.2 km² (65.4%) to 51.2 km² (41.5%). And finally, the NF area also decreased in percentage change by –7.1% from 14.7 km² (11.2%) to 2.6 km² (4.1%). These above declines in both the LF and NF areas were attributed to anthropogenic activities such as degradation, poor management of the experimental plots, and legal fellers.

Table 6: *Changes in land cover of Gambari Forest Reserve from 1984 to 2004*

Classes	Area in 1984 (km²)	Area in 1984 (%)	Area in 2004 (km²)	Area in 2004 (%)	Percentage Change from 1984–2004
NF	14.70	11.20	37.80	25.10	13.90
LF	79.20	65.40	51.20	43.70	–21.70
DF	31.70	23.40	36.60	31.20	7.80

Table 7: *Changes in land cover of Gambari Forest Reserve from 2004 to 2020*

Classes	Area in 2004 (km²)	Area in 2004 (%)	Area in 2020 (km²)	Area in 2020 (%)	Percentage Change from 2004–2020
NF	37.80	25.1	2.60	4.10	–21.00
LF	51.20	43.7	51.20	41.50	–2.20
DF	36.60	31.20	72.80	54.40	23.20

Table 8: *Changes in land cover of Gambari Forest Reserve from 1984 to 2020*

Classes	Area in 1984 (km²)	Area in 1984 (%)	Area in 2020 (km²)	Area in 2020 (%)	Percentage Change from 1984–2020
NF	14.70	11.20	2.60	4.10	–7.10
LF	79.20	65.40	51.20	41.50	–23.90
DF	31.70	23.40	72.80	54.40	31.00

Conclusions

It is very important to study LULC changes due to natural causes such as climate variability or climate change, resulting in floods, drought, or anthropogenic causes, such as industrialisation and urbanisation. LULC analysis can provide important information for global environment change and sustainable development studies, which can also be useful for decision-makers. A long time series (1984, 2004, and 2020) of RS images with a resolution of 30 m were used in the present research. Findings show that the Gambari Forest Reserve area in 1984 had a total DF cover of 31.7 km^2, while LF covered 79.2 km^2, and NF covered 14.7 km^2, representing 23.4%, 65.4%, and 11.2%, respectively, of the land area. In sum, the LULC classification using Landsat imagery of 1984 reveals that LF occupied the largest area size both in percentage and kilometre due to the fact that the forest was still intact, devoid of deforestation.

In 2004, in the Gambari Forest Reserve, DF covered an area of 36.6 km^2, while LF covered 51.2 km^2, and NF covered 37.8 km^2, representing 31.2%, 43.7%, and 25.1%, respectively. In 2004, DF area increased by 7.8%. LF showed a reduction in both the percentage and area size in 2004 compared to the previous year studied (1984) due to the effects of deforestation. A summary of the findings in 2004 shows that LF still has the highest area and percentage cover.

Finally, in 2020, DF covered an area of 72.8 km^2, while LF covered 51.2 km^2 and NF covered 2.6 km^2, representing 54.4%, 41.5%, and 4.1%, respectively. To summarise, DF had the highest percentage and area cover size in 2020.

Many more reasons (also explained in the literature review) show clearly how LULC study is important for policy making and making decisions to prevent environmental degradation. There are many techniques that can be used in monitoring and assessment of LULC, such as RS and GIS.

Therefore, it is recommended that the concept of using satellite images of land cover change demonstrated the extent and status of land cover. Therefore, this study recommends that more efforts need to be taken seriously to halt deforestation and any other human activities that can have negative impacts on forests. In the near future, more studies should be conducted to complement the deployment of an integrated RS–GIS approach towards precision carbon management.

References

[1] Dafang, Z., Yunfeng, H., Batunacun, L.Z. (2019): Assessment of land-use and land-cover change in Guangxi, China. *Scientific Reports*, 9(1), pp. 1–13, DOI:10.1038/s41598-019-38487-w.

[2] Lambin, E.F. et al. (2001): The causes of land-use and land-cover change: moving beyond the myths. *Global Environmental Change*, 11, pp. 261–269.

[3] Sohoulande Djebou, D.C. (2017): Spectrum of climate change and streamflow alteration at a watershed scale. *Environmental Earth Sciences*, 76(19), pp. 1–13.

[4] Verburg, P.H., Chen, Y., Veldkamp, T.A. (2000): Spatial explorations of land use change and grain production in China. *Agriculture, Ecosystems & Environment*, 82(1–3), pp. 333–354, DOI:10.1016/S0167-8809(00)00236-X.

[5] Diouf, A., Lambin, E.F. (2001): Monitoring land-cover changes in semi-arid regions: remote sensing data and field observations in the Ferlo, Senegal. *Journal of Arid Environments*, 48(2), pp. 129–148, DOI: 10.1006/jare.2000.0744.

[6] Akram, M., Qian, Z., Wenjun, L. (2008): Policy Analysis in Grassland Management of Xilingol Prefecture, Inner Mongolia. In: *The Future of Drylands,* Lee, C., Schaaf, T. (eds.). Springer: The Netherlands, pp. 493–505, DOI:10.1007/978-1-4020-6970-3_45.

[7] Li, Y., Liu, Y. (2011): The Ecological Analysis of a New Round Land Use Planning Based on Ecological Footprint in Guangxi. In: *Proceedings of the 2011 2nd International Conference on Mechanic Automation and Control Engineering*, Hohhot, China, IEEE: China, pp. 6981–6984, DOI 10.1109/MACE.2011.5988655.

[8] Pielke, R.A. Sr., Pitman, A., Niyogi, D., Mahmood, R., McAlpine, C., Hossain, F. (2011): Land use/land cover changes and climate: modeling analysis and observational evidence. *Wiley Interdisciplinary Reviews Climate Change*, 2(6), pp. 828–850, DOI:10.1002/wcc.144.

[9] Reis, S. (2008): Analyzing land use/land cover changes using remote sensing and GIS in Rize, North-East Turkey. *Sensors*, 8(10), pp. 6188–6202, DOI:10.3390/s8106188.

[10] Srivastava, P.K., Singh, S.K., Gupta, M., Thakur, J.K., Mukherjee, S. (2013): Modeling impact of land use change trajectories on groundwater quality using remote sensing and GIS. *Environmental Engineering and Management Journal,* 12(12), pp. 2343–2355, DOI:10.30638/eemj.2013.287.

[11] Pradhan, B., Lee, S., Mansor, S., Buchroithner, M., Jamaluddin, N., Khujaimah, Z. (2008): Utilization of optical remote sensing data and geographic information system tools for regional landslide hazard analysis by using binomial logistic regression model. *Journal of Applied Remote Sensing*, 2(1), pp. 1–11, DOI:10.1117/1.3026536.

[12] Singh, S.K., Laari, P.B., Mustak, S., Srivastava, P.K., SzaboÂ, S. (2017): Modelling of land use land cover change using earth observation data-sets of Tons River Basin, Madhya Pradesh, India*. Geocarto International,* 33(11), pp. 1–34, DOI:10.1080/10106049.2017.1343390.

[13] Hua, A.K. (2017): Land use land cover changes in detection of water quality: a study based on remote sensing and multivariate statistics. *Journal of Environmental and Public Health,* 2017(1), pp. 1–12, DOI:10.1155/2017/7515130.

[14] Olokeogun, O.S., Iyiola, K., Iyiola, O.F. (2014): Application of remote sensing and GIS in land use/land cover mapping and change detection in Shasha forest reserve, Nigeria. *ISPRS – International Archives of the Photogrammetry, Remote Sensing and Spatial Information Sciences*, Volume XL-8, pp. 613–616, DOI:10.5194/isprsarchives-XL-8-613.

[15] Rai, P.K., Vishwakarma, C.A., Thakur, S., Kamal, V., Mukherjee, S. (2016): Changing land trajectories: a case study from India using a remote sensing-based approach. *European Journal of Geography*, 7(2), pp. 63–73.

[16] Khan, S., Qasim, S., Ambreen, R., Syed, Z. (2016): Spatio-temporal analysis of landuse/landcover change of district Pishin using satellite imagery and GIS. *Journal of Geographic Information System*, 8(3), pp. 361–369.

[17] Zeleke, G., Hurni, H. (2001): Implications of land use and land cover dynamics for mountain resource degradation in the Northwestern Ethiopian Highlands. *Mountain Research and Development*, 21(2), pp. 184–191, DOI:10.1659/0276-4741(2001)021[0184: IOLUAL] 2.0.CO; 2.

[18] Adedeji, O.H., Tope-Ajayi, O.O., Abegunde, O.L. (2015): Assessing and predicting changes in the status of Gambari Forest Reserve, Nigeria using remote sensing and GIS techniques*. Journal of Geographic Information System*, 7(3), pp. 301–318, DOI:10.4236/jgis.2015.73024.

[19] Whitmore, T.C. (1993): *An Introduction to Tropical Rain Forest*, 2nd edition*.* Oxford University Press: United States, 296 p.

[20] Sanwo, S.K., Ige, P.O., Sosanya, O.S., Ogunlaye, O.G. (2015): Tree species diversity and forest stands dynamics in a tropical rainforest in Southern Nigeria. *Malaysia Applied Biology Journal*, 44(2), pp. 65–73.

[21] Larinde, S.L., Olasupo, O.O. (2011): Socio-economic importance of fuelwood production in Gambari forest reserve area, Oyo State, Nigeria. *Journal of Agriculture and Social Research (JASR)*, 11(1), pp. 201–210.